SEMMELWEIS EGYETEM

DOKTORI ISKOLA

Ph.D. értekezések

2860.

JUHÁSZ ÁKOS GYÖRGY

Celluláris és molekuláris biofizika
című program

Programvezető: Dr. Kellermayer Miklós, egyetemi tanár

Témavezetők: Dr. Jedlovszky-Hajdú Angéla, egyetemi docens

Dr. Smeller László, egyetemi tanár

3D ARTIFICIAL MATRICES FOR BIOMEDICAL PURPOSES; SYNTHESIS AND SPECTROSCOPIC CHARACTERISATION

Ph.D. thesis

Ákos György Juhász

Doctoral School of Theoretical and Translational Medicine

Semmelweis University

Supervisors: Angéla Jedlovszky-Hajdú Ph.D.
László Smeller DSc.
Abdenacer Idrissi Ph.D.

Official reviewers: Sophie Fourmentin Ph.D.
István Szilágyi Ph.D.

Head of the Complex Examination Committee: György Losonczy, DSc.
Members of the Complex Examination Committee:
Andrea Székely DSc.
Ákos Jobbágy DSc.

Budapest
2023

University of Lille

Faculty of Sciences and Technologies

Doctoral School 104 - Science of the Matter, of the Radiation, and of the Environment

Doctoral Thesis

by

Ákos György JUHÁSZ

to obtain the degree of

Doctor of Lille University

Discipline: Physical, analytical, and theoretical chemistry

3D Artificial Matrices for Biomedical Purposes; Synthesis and Spectroscopic Characterisation

Date of defense: 26 May 2023

Sophie	**Fourmentin-Lamotte**	**Referee**
	Professor, Université du Littoral-Côte d'Opale	
István	**Szilágyi**	**Referee**
	Associate Professor, University of Szeged	
Abdenacer	**Idrissi**	**Co-supervisor**
	Professor, University of Lille	
Angéla	**Jedlovszky-Hajdú**	**Co-supervisor**
	Associate Professor, Semmelweis University	
Frédéric	**Affouard**	**Examiner**
	Professor, University of Lille	
Natalia	**Correia Teixera**	**Examiner**
	Associate Professor, University of Lille	
Miklós	**Kellermayer**	**Examiner**
	Professor, Semmelweis University	
Romána	**Zelkó**	**Examiner**
	Professor; Semmelweis University	

Université de Lille

Faculté des Sciences et Technologies

Ecole Doctorale 104 - Sciences de la Matière, du Rayonnement, et de l'Environment

Thèse de Doctorat

par

Ákos György JUHÁSZ

pour l'obtention du titre de

Docteur de l'Université de Lille

Discipline : Chimie théorique, physique, analytique

Synthèse et caractérisation par spectroscopie de vibration de polymère pour une application biomédicale

Date de soutenance : 26 mai 2023

Sophie	**Fourmentin-Lamotte**	**Rapporteur**
	Professeur, Université du Littoral-Côte d'Opale	
István	**Szilágyi**	**Rapporteur**
	Professeur associé, Université de Szeged	
Abdenacer	**Idrissi**	**Co-directeur de thèse**
	Professeur, Université de Lille	
Angéla	**Jedlovszky-Hajdú**	**Co-directrice de thèse**
	Professeur associé, Université Semmelweis	
Frédéric	**Affouard**	**Examinateur**
	Professeur, Université de Lille	
Natalia	**Correio Teixera**	**Examinateur**
	Maître de conférences, Université de Lille	
Miklós	**Kellermayer**	**Examinateur**
	Professeur, Université Semmelweis	
Romána	**Zelkó**	**Examinateur**
	Professeur, Université Semmelweis	

Table of Contents

List of Abbreviations

∠cation …O=C	The angle between the cation and the O=C group
2D	Two-dimensional
3D	Three-dimensional
ATR-FTIR	Attenuated Total Reflectance Fourier Transform Infrared Spectroscopy
DFT	Density Functional Theory
DMF	Dimethylformamide
ECM	Extracellular matrix
MD	Molecular Dynamics
NN	Nearest neighbor analyses
Od, Hd,	The oxygen atom of DMF, the Hydrogen atom of DMF
Ow, Hw	The oxygen atom of water, the Hydrogen atom of water
PASP	Poly(aspartic acid)
PSI	Polysuccinimide
RDF	Radial Distribution Function
SEM	Scanning Electron Microscopy
VP	Voronoi Polyhedra

1. Introduction

1.1. Biomaterials, Regenerative medicine

The desire to replace lost body parts has been a part of human history since the beginning. In ancient times biomaterials were already used, such as gold for dental implants; the Mayans created implants from seashells, or, as you can see in Figure 1.1, a wooden toe was used after an amputation in Egypt. [1,2] However, modern advances can be traced back to the 1950s and 1960s, with the development of synthetic materials, such as polymers, metals, and ceramics, for use in medical purposes. The first synthetic implantable material, Polyethylene was used for the first time as a ball-and-socket joint replacement for the hip by Sir John Charnley. [3] A modern version can be seen in Figure 1.1. This was a significant advancement in orthopedic surgery, providing a durable and long-lasting solution for patients with hip joint disorders. In the 1970s, scientists began to develop new types of synthetic materials, such as silicone, which could be used in soft tissue implants, such as breast implants. This marked a significant advancement in the field of plastic and reconstructive surgery. [4] In the 1980s, scientists began developing new ceramic and metal materials, such as titanium and zirconia, that could be used for dental implants and joint replacements. [5]

Figure 1.1 Technical advances of using biomaterials through history, a) a wooden toe from Egypt that was used after an amputation (1065–740 BC) b) hip implant that uses different synthetic materials combined to give the best usability, c) a carefully fabricated metal stent into small vessels d) bone graft that uses a conventional prosthetic component and a tissue engineering approach to regenerate spinal tissues [1]

In recent years, biomaterials have continued to evolve with the development of new technologies, such as 3D printing, which allows for the creation of customized implants and prosthetic devices. Additionally, new materials are developed, such as hydrogels and nanofiber-based meshes that can mimic the properties of natural tissues. A more advanced approach is combining different materials to add extra

functionalities.[4,5] An example can be seen in Figure 1.1, where they produced a bone graft with a conventional metallic component filled with a collagen sponge to enhance tissue regeneration. [1]

Defining biomaterials is quite challenging since they are a vast group of materials with little, if any, physical or chemical similarity. The name refers to the intended use and not the material type itself. The sole purpose of biomaterials is to be used in medicine to reconstruct or repair damaged tissues or body parts, improving the patient's quality of life. This field grew into a multidisciplinary area over the years, where all kinds of scientific approaches are needed to create complex engineering solutions with properties to contact or interact with a biological system and replace a physiological function in the human body. They can be used as implants or implantable medical devices, for example, simple as a stent or a dental implant or more complex solutions like a pacemaker. [5,6]

The field of medicine that focuses on the repair or replacement of damaged cells, tissues, and organs is called Regenerative medicine. It contains various approaches and technologies, including cell-based therapies, tissue engineering, and gene therapy. Cell-based therapies involve using stem cells, undifferentiated cells that can develop into many different types of cells. These cells can repair or replace damaged cells and tissues, providing new hope for patients with conditions such as cancer, heart disease, and diabetes. [3]

1.1.1 Tissue engineering

Tissue engineering is a rapidly growing field that aims to repair or replace damaged or diseased tissues using a combination of biological and engineering principles. The goal of tissue engineering is to develop functional tissue constructs that can repair or replace lost or damaged tissues in the human body, such as bones, cartilage, blood vessels, and nerves. The field of tissue engineering involves using cells, biomaterials, and bioactive molecules to create functional tissue constructs. Cells are typically obtained from the patient or a tissue donor, then cultured and expanded in the laboratory. Once the tissue construct is created, it is typically implanted into the patient's body, where it can begin to function and integrate with the surrounding tissue. Some of the most promising areas of tissue engineering include the repair of bone, cartilage, and heart valves and the engineering of blood vessels and nerve tissue. Tissue engineering can also be used to

develop new medical devices, such as artificial organs, and new therapies for diseases like cancer. Tissue engineering can also be used to create in vitro models of diseases, which can be used to study disease mechanisms and test new therapies. [5,7]

1.1.2 Properties of Biomaterials

When using such materials, the initial property is bio-inertness to avoid any unwanted secondary interactions like inflammation or blood coagulation. When designing biocompatible materials to restore tissue function (prosthetic implants, bioresorbable sutures, and artificial grafts), one must consider that various tissues contain different physical, biological, and biochemical properties. Therefore, the material's composition, degradation kinetics, and material-cell interaction are vital factors. These materials can be derived from synthetic or natural routes as well. Additionally, several physicochemical properties needed to be met for the intended application. Such as biocompatibility, biodegradability, mechanical properties, stability, structural properties, processability (how easily the material can be shaped or formed into an applicable shape), and porosity. [5,8]

Biocompatible property is also a very important to perform a function without any harmful immune or inflammatory reaction. It is most important when a scaffold interacts with a biological system and cellular functions such as adhesion, proliferation, migration, and differentiation occur. Since different materials and use cases have other limits on achieving biocompatibility [5,9,10]

Biodegradability refers to the degradation of the biomaterial over time of tissue regeneration. Also, these materials, while undergoing degradation, must assist in the healing and renewal of the concerned area. One should consider that body fluids contain dissolved oxygen and other oxidants, so the surface must have good corrosion resistance or some protective coating. [4,5,11,12]

Different types of tissues require other mechanical properties like tensile strength, Young modulus, fatigue strength, toughness, and elasticity, so before selecting a biomaterial, one should consider that it's ideally fit for that purpose. The mechanical property of the biomaterial needs to be very close to the material it replaces. [5,6,13,14]

Structural properties, for example, the size or shape of the used material, play an essential role in different applications. For example, to enable cell attachment, the

scaffold needs to have a high surface-to-volume ratio to allow cell attachment or sufficient drug release. [5–7,15]

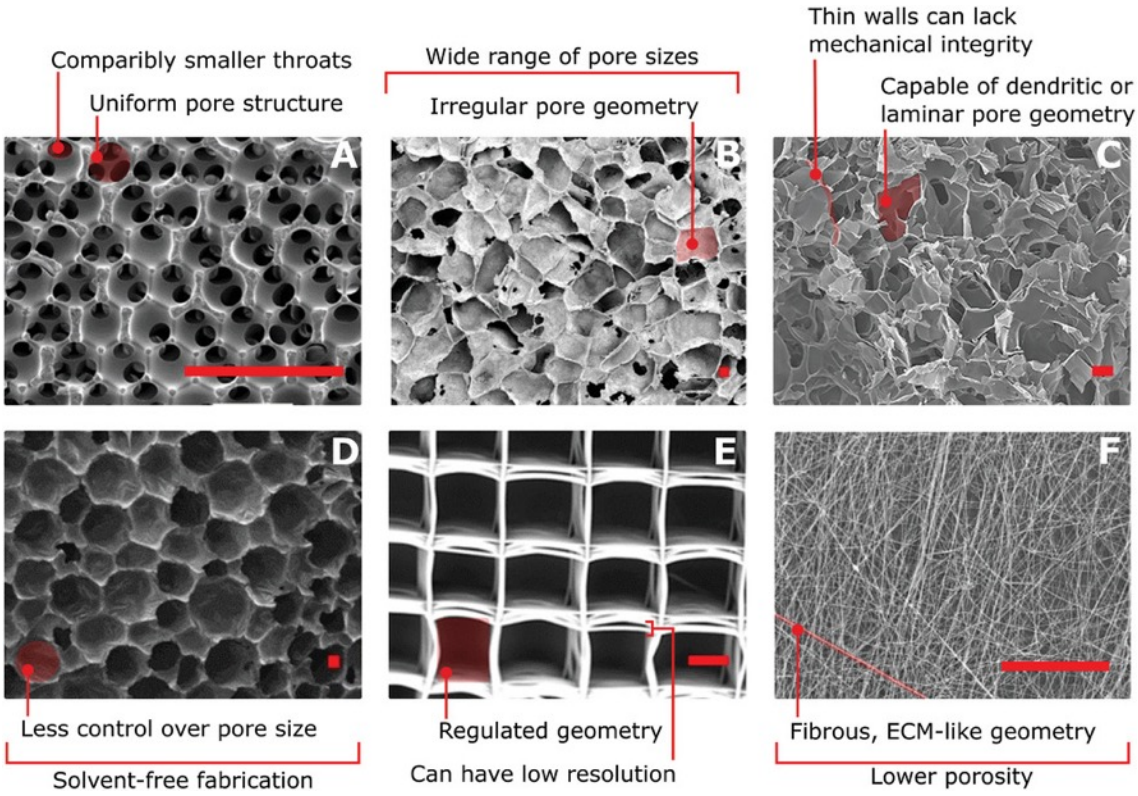

Figure 1.2 SEM images of different porous structures made by A) sphere templating, B) salt-leaching, C) freeze-drying, D) gas-foaming, E) 3D-printed via melt electrospinning writing, F) conventional electrospinning. Scale bars are 100 µm. [16]

The scaffold's porosity determines how the cell can migrate and affects the platform's flexibility (Figure 1.2). Increased porosity lowers the protection against corrosion. When discussing processability, one should consider if it's easily fabricated to a desired shape or if it is easy to handle. Stability is a fundamental property also when choosing a biomaterial because it should not change its physicochemical properties in the biological environment. [4,16–18]

1.1.3 Polymers

Polymers are macromolecules with high molecular mass, ranging from a few thousand to millions of monomer units. They are made up of many structural elements by covalent bonding. In medicine, implants, contact lenses, single-use medical devices, and even drug carriers are made of some kind of polymer. [19–21]

Biopolymers are polymers that occur naturally and can be used in biological systems. To create artificial polymers for use in medicine, the basis should be derived from biopolymers that are also found in the human body. Such preparations, as we have seen above, are expected to be biocompatible and biodegradable. Poly(aspartic acid), which is the subject of intensive research in the Nanochemistry Research Group (Semmelweis University), could be a good choice as a polymer for use in medicine. [22–25]

Polysuccinimide (PSI) is an anhydride of poly(aspartic acid) (PASP), which can be synthesized from aspartic acid using a green chemistry process (solvent-free) with a phosphoric acid catalyst. The chemical formulae of the different stages are shown in Figure 1.2 [23,26]

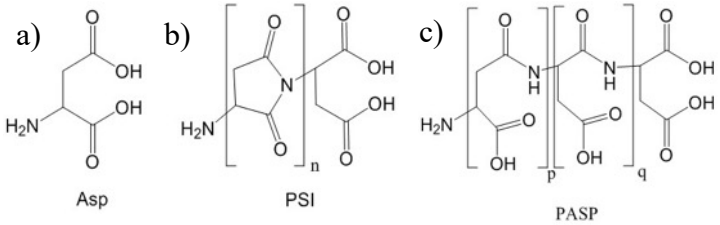

Figure 1.2. The chemical formula of a) Aspartic acid, b) Polysuccinimide, and c) Poly(aspartic acid) [26]

The reactivity of polysuccinimide is very high due to the amide ring, so that it readily reacts with nucleophilic reagents even at room temperature without the presence of a catalyst. The solvent of polysuccinimide is dimethylformamide (DMF) or dimethyl sulfoxide (DMSO). Polysuccinimide does not react with alcohols, but it reacts with hydroxide ions. Hydrolysis yields two monomeric units, α and β aspartic acid. This hydrolysis occurs spontaneously in a mildly alkaline environment and can be initiated even at a pH of 7.4. In the body, the two monomeric units of protein L-iso aspartyl (D-aspartyl) can be converted into the α and β forms by the enzyme O-methyltransferase (PIMT). An important result of the reaction is that the hydrophobic polymer becomes hydrophilic, i.e., the polymer becomes water-soluble. [22,27,28]

1.2. Electrospinning

1.2.1. A short history of electrospinning

The electrospinning technique is a method used to create micro or nanofiber-based meshes that resemble the extracellular matrix (ECM) of natural tissues. This is important in tissue engineering, where cells are placed on a scaffold that will hold them and could be a base for their structural network, like the native ECM. John Francis Cooley filed the first patent for an electrospinning device in 1899. They proposed four different heads for electrospinning, including a conventional head, a coaxial head, an air-jet head, and a rotary spinning head.[29–31]

Anton Formhals made significant advances in the field in the 1930s and 1940s by refining the arrangement of the components of the electrospinning device and controlling the length and diameter of the fibers produced. Sir Geoffrey Ingram Taylor also made essential contributions in the 1960s by establishing a mathematical model for the cone phenomenon in electric fields, which is now known as the Taylor cone.[30,32]

In the 1970s, Peter K. Baumgarten devised a method to photograph the fibers produced by electrospinning during their flight through the air and investigated the parameters that influence the formation of fibers, such as viscosity, flow velocity, and tension. The real progress in the field began in 1993, when Jayesh Doshi and Darrel H. Reneker discovered that fibers with a diameter of nanometers could be created easily in electrospinning studies. Since then, research in the field has grown rapidly, with more than 100 types of polymers used to create fibrous structures from synthetic, and natural polymers, and blends.[29,30]

In recent years, significant advancements have been made in the optimization of apparatus design and process parameters, including the use of salts to improve the electrospinnability of polymers. [33–35]

The use of electrospinning in the field of medicine is increasing, as it has the potential to revolutionize the way we create replacement tissues and organs, as well as drug delivery systems (Figure 1.3). With continued research and development, it has the potential to improve the quality of life for patients suffering from chronic conditions and injuries. [22,36]

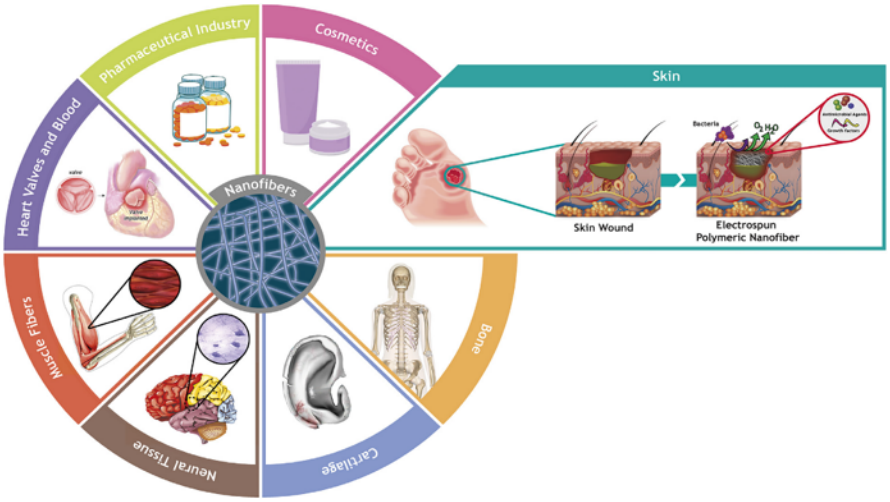

Figure 1.3 Applications of electrospinning in medicine [37]

1.2.2. Electrospinning setup

The technique of electrospinning is a method for creating nano- and microfibers. The main components of an electrospinning setup include a container filled with a viscous polymer solution, a high-voltage power supply, a spinneret (typically a syringe needle), and a collector to collect the randomly aligned fibers. A schematic of the process can be seen in Figure 1.4 Schematic of the electrospinning process. [24,38]

The positive pole of the high-voltage power supply is connected to the syringe needle, creating a potential difference between the needle and the grounded collector that generates an electrical field. The flow rate of the polymer solution emerging from the syringe can be controlled by a syringe pump. A thin polymer drop forms at the end of the syringe needle and undergoes a whipping motion as it is propelled toward the collector. Ideally, the solvent evaporates on its way, leaving behind a dry, solvent-free, spider-web-like structure on the collector. [31,39]

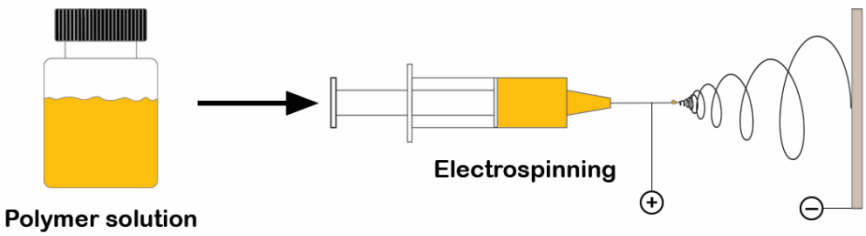

Figure 1.4 Schematic of the electrospinning process [24]

Several parameters influence the electrospinning process and the properties of the resulting fibers. One of the most important parameters is the concentration of the polymer solution. Fiber formation does not occur at low concentrations, and electrostatic spraying results in the formation of micro or nanodroplets or particles (Figure 1.5). As the concentration increases, fibers begin to appear in addition to droplets. At optimal concentrations, a homogeneous fibrous structure is obtained. If the concentration is increased further, helical ribbons are formed. The viscosity of the solution can also be adjusted by varying the concentration. [31,38,40]

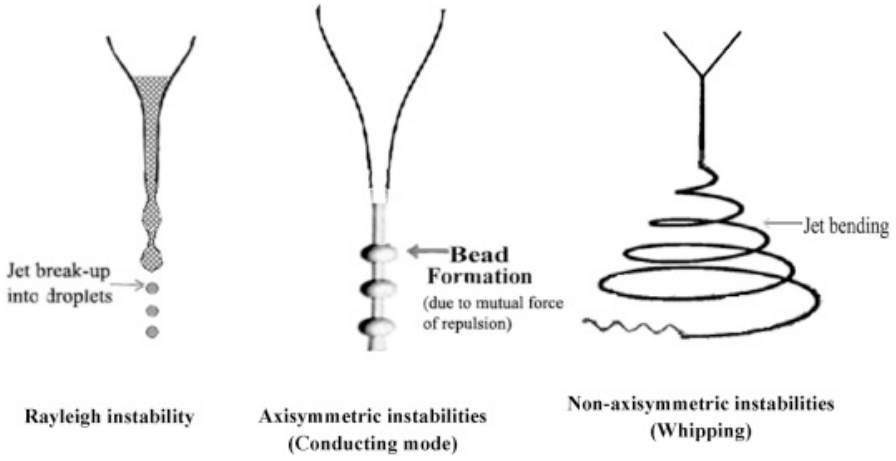

Figure 1.5. Different instabilities during electrospinning [41]

Another critical parameter in electrospinning is the viscosity of the polymer solution. Low viscosity is not ideal for producing continuous, smooth fibers, but a viscosity that is too high can also be problematic, as it can make it difficult to "repel" the fibers between the fiber-forming head and the collector. The molecular weight of the polymer also plays a role in determining the viscosity of the solution. Droplet formation occurs below a specific molecular weight when the concentration is fixed. Above the value required for fiber formation, ribbons are formed. If the molecular weight is too high, ribbons can be formed even at low concentrations. Additionally, the surface tension of the solution can affect both the viscosity and the morphology of the fibers. [38,42–44]

During electrospinning, the polymer solution polarizes due to the high electric field. Free electrons, ions, or ion pairs will carry charges within the liquid, and an electrical double layer will form due to ion mobility. The conductivity of the solution depends on the polymer, the solvent, and any additional additives. In general, natural polymers are polyelectrolytes, so as the ions increase, the charge-carrying capacity of the polymer increases, requiring a higher applied voltage, which in turn results in poorer

electrospinnability compared to synthetic polymers. The conductivity can be adjusted by adding different salts, secondary solvents, or nanoparticles. In general, increasing conductivity can result in thinner fibers. [44–49]

Conductivity can be adjusted by adding different salts, which can also influence the diameter of the fibers, and reduce droplet formation. Adding specific salts can also change the surface tension of the solution and result in fiber formation. For example, adding KCl to an aqueous solution of poly(vinyl alcohol) can increase the conductivity of the solution and result in larger fiber diameters. On the other hand, adding NaCl or $CaCl_2$ to the system can result in fibers with smaller diameters than those obtained with LiCl. Overall, the electrospinning process depends on a delicate balance of parameters that must be carefully optimized to achieve the desired fiber properties. [50–52]

Nowadays, the creation of fibrous structures combined with nanoparticles is receiving increasing attention. By adding silver nanoparticles, for example, an artificial mesh system can be created that gives an antibacterial effect to the resulting fibrous structure or even results magnetic properties by adding magnetite. [46,53,54]

The success of the electrospinning process depends on the optimal parameters of the various components involved in the formation of the fibers. These parameters interact with each other, making it a time-consuming process to optimize them. Some of the key influencing factors include the material properties of the solution, such as the solvent-polymer concentration, viscosity, conductivity, surface tension, dielectric constant, and solvent volatility. These parameters can affect the viscosity, diameter of the fibers, and droplet formation. The molecular weight of the polymer and the concentration of the polymer in the solution can also affect the viscosity and the amount of the final product. [55–57]

The formation of fibers during electrospinning is influenced by several experimental parameters that are not related to the material properties of the polymer, but rather to the configuration of the equipment. These include the electrostatic potential, the electric field's strength, the electrostatic field's shape, the diameter of the syringe needle or orifice used to dispense the solution, the flow rate of the solution, and the distance between the needle and the target. As the applied voltage increases, the diameter of the fibers decreases, resulting in an increase in the volume of the final product. If the flow rate is too low, the Taylor cone is not formed; if it is too high, pulsation occurs. The

distance between the needle and the target can also affect the diameter and morphology of the fibers. If the distance is too short, the solvent cannot evaporate properly, and the fibers do not have time to solidify. In addition to these parameters, environmental conditions such as temperature, humidity, pressure, airflow, and air composition can also affect fiber formation. Temperature primarily affects viscosity, which can decrease the diameter of the fibers, but it can also impact other parameters. Humidity primarily affects the evaporation of the solvent, which can affect the porosity of the fibers. Due to these complexities, it is important to conduct experiments under strict conditions to ensure reproducibility, as small changes in parameters can result in significant changes in the final fiber formation outcome. [31,38,50,56,57]

It was previously mentioned that the electric field applied to a liquid droplet must reach a specific potential value for the droplet to take on a cone-like shape and for fiber formation to occur. However, the impact on fiber diameter is still debated, as it can vary depending on the polymer and its concentration. Care must also be taken when selecting the flow rate of the polymer solution, as it affects the amount of time the solution spends in the syringe before polarizing. A lower flow rate is typically preferred, but droplet formation and thicker fibers will result if it is too high. The distance between the target and the fiber-forming head can also affect fiber diameter, but it must fall within a specific optimal range. If the distance is too close, the solvent will not have enough time to evaporate, and if it is too far, beads will form. Factors such as the volatility of the solvent and environmental conditions, such as temperature, humidity, pressure, airflow, and air composition, must also be considered. These conditions can significantly impact the effectiveness of fiber formation and can affect parameters such as viscosity and porosity. It is essential to carefully consider all of these factors to produce fibers with the desired properties consistently. [38,58–60]

Additionally, the choice of polymer solution also plays a crucial role in the fiber formation process. Different polymers have different properties, such as viscosity, conductivity, and solubility, that can affect the final fiber properties. For example, a polymer with high viscosity may lead to thicker fibers, while a polymer with low conductivity may require a higher electric field to achieve fiber formation. Therefore, it is important to carefully select the polymer solution that is most suitable for the desired application. [60,61]

Furthermore, the choice of solvent also plays a vital role in the fiber formation process. The solvent must be able to dissolve the polymer and should have a low boiling point to allow for easy evaporation. The volatility of the solvent should also be considered, as a more volatile solvent will evaporate faster and affect the porosity of the fibers. Additionally, the solvent should not react with the polymer or any other materials that may be present in the system. [31,44,57]

In conclusion, the fiber formation process is a complex process that involves various parameters that must be carefully considered. The applied electric field, the flow rate of the polymer solution, the distance between the target and fiber forming head, the choice of polymer solution, and the choice of solvent all play essential roles in determining the final fiber properties. Therefore, due care must be taken when applying this technique and setting the parameters to ensure that the desired properties of the final product can be consistently reproduced.

1.2.3. Different fiber formation arrangements

Electrospinning is a widely used method for creating single or composite polymer nanofibers in research settings. This technique utilizes an electric field to produce fibers that are collected on a flat target, resulting in a thin film-like layer. The technique is relatively simple to implement however, its productivity is low, and it is not suitable for large-scale production. The resulting fibers can be randomly oriented or unidirectionally oriented using different targets or auxiliary electrodes. Unidirectionally oriented nanofibers exhibit higher mechanical strength and unique optical and electrical properties.[62,63] To increase productivity, multiple needles can be used, but this can lead to uneven deposition and a non-uniform electric field between the needles. Clogging of the syringe needle is a common problem in electrospinning, leading to inconsistent fiber production and reduced productivity. To overcome this limitation, various needle-free techniques have been developed, such as centrifugal fiber formation and rotating roller targets (Figure 1.5). [64–68] One example is centrifugal fiber formation, which is commonly used in cotton candy production and can be supplemented with an electric field to produce fibers of a few hundred nanometers at low tension and low speed. [64,69,70]

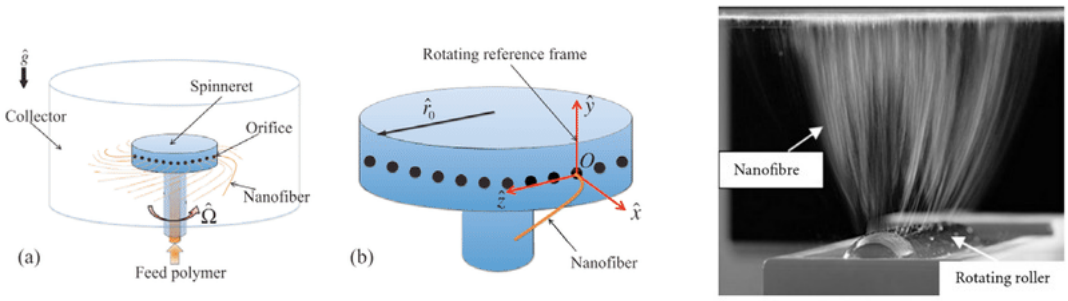

Figure 1.5 Schematic of a centrifugal fiber formation apparat [64] *and a rotating roller-based needless electrospinning design* [65]

The geometry of the target plays a crucial role in the orientation of the fibers. The use of a rotating drum target is becoming increasingly popular, as it not only facilitates the orientation of fibers but also leads to a more homogeneous fiber distribution than a flat collector. When the rotating drum is rotated at a high enough speed, the fibers will be arranged parallel to each other on the target. In cases where the use of a rotating drum alone does not lead to orientation, a target made up of parallel wires in a cylindrical shape can be used to achieve the orientation of stretched fibers between the wires. However, it is important to note that the orientation of fibers is dependent on the combination of optimal polymer properties, concentration, temperature, humidity, and flow rate.[63,71]

The resulting fibrous structure can be functionalized with nanoparticles, such as for antibacterial effects or by adding carbon nanotubes to enhance the mechanical properties or create electrically conductive fibers. Additionally, the conductivity and viscosity can be controlled by adding salts to increase the formability of the fibers and influence the resulting fiber diameter. Furthermore, adding salts can also lead to orientation and the formation of spider web-like nanostructures between the fibers. [46,47,53,72,73]

Cotton candy-like three-dimensional expansions have also been observed in the presence of various additives. Although there is increasing interest in such structures, the exact cause of their formation has not yet been fully understood. It is thought to be related to the accumulation of charges, the interaction of solution components, or the effect on the electric field. Using an electrostatic lens, the fibers accumulate in a smaller area, accelerating the formation process. Additionally, 3D printing has also been used to give different shapes to the 3D structure that is formed. [74–77]

As discussed before, in electrospinning, a huge number of parameters are involved in the creation of the final product with a desirable outcome. Computer simulations can be used to aid optimization and to characterize and understand the processes at molecular levels.

1.3. Molecular modeling

In the course of my thesis work, I was led during my stay at the University of Lille to use molecular modeling (as well as vibrational spectroscopy) in particular for two problems. The first one concerns the use of DFT calculations to help interpret the infrared spectra of salts/DMF solutions that I recorded during my stay at the University of Lille. The second concerns the analysis of the local structure in the DMF/water mixture using molecular dynamics. I will therefore start in this part to give the general principles of these methods (Figure 1.6).

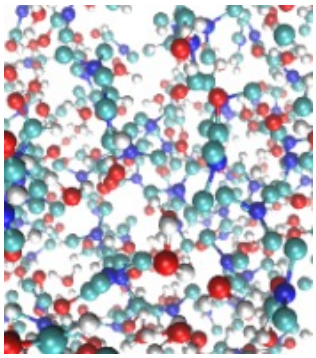

Figure 1.6 A close view inside a simulation box of DMF-water

Molecular modeling is the use of computer simulations to study the structure and behavior of molecules. It is a powerful tool for understanding the properties of molecules and predicting their behavior in different environments. Molecular modeling techniques include molecular dynamics, which simulates the motion of atoms and molecules over time, and quantum mechanics-based methods, which use the principles of quantum mechanics to predict the electronic structure of molecules. These techniques are used in a wide range of fields, including drug design, materials science, and biochemistry.

It is important to note that the accuracy of molecular modeling predictions depends on the quality of the input data, the method used, and the assumptions made during the simulation. Therefore, it is crucial to validate the predictions made by molecular modeling against experimental data. Additionally, as the complexity of the

systems increases, the computational cost of molecular modeling simulations also increases, making it important to choose the most appropriate method for the system under study and to use high-performance computing resources.

Molecular dynamics (MD) simulation is a computational method that uses Newton's laws of motion to simulate the movement of atoms and molecules over time. It is based on the idea that the motion of atoms and molecules can be predicted by solving the equations of motion for each atom or molecule in a system. The interactions between atoms are usually described using force fields, which are mathematical models that describe the potential energy of the system based on the positions of the atoms. These force fields can include in additions to intermolecular interactions terms for intra molecular interactions that include bond stretching, bond bending, dihedral angles, and non-bonded interactions. The corresponding parameters are calculated using quantum mechanics. In fact, in MD simulation, a system is modeled as a collection of atoms or molecules, and the initial positions and velocities of the atoms or molecules are specified. The simulation is then run for a specified period of time, and the positions and velocities of the atoms or molecules are calculated at each time step. Various statistical functions are calculated to help study the system's behavior over time, including the structure and dynamics of the studied system. It is worth noting that these methods require significant computational resources and expertise in mastering the command language interpreter (shell) and programming to run and in statistical physics to interpret the results.

MD simulation can be used to study a wide range of properties of molecules and materials, including their stability, reactivity, and conformational changes. It can also explore the interactions between molecules, such as protein-ligand binding and protein-protein interactions. MD simulation can also be used to study the properties of large biological systems, such as proteins and nucleic acids, and to investigate the mechanism of enzyme catalysis and protein folding.

One of the key advantages of MD simulation is its ability to study the dynamics of a system over time. This can provide insights into the mechanisms of chemical reactions and biological processes and can be used to design new drugs and materials. Additionally, MD simulations can provide a molecular-level understanding of the behavior of a system, which can be used to make predictions about the properties of the

system that are difficult to study experimentally, but it is essential to validate the predictions made by MD simulation.

Quantum calculation methods are computational techniques that use the principles of quantum mechanics to predict the electronic structure and properties of molecules and materials. These methods are based on the idea that the behavior of electrons in a system can be described using quantum mechanical wave functions, which are mathematical functions that describe the probability of finding an electron in a particular location in space. There are several different quantum calculation methods that can be used to study different types of systems. Some of the most used methods are Hartree-Fock (HF), Ab initio, and Density Functional Theory (DFT). HF is a method that describes the electronic structure of a molecule using a single determinant wave function. It is a widely used method for predicting the electronic structure of small molecules. [78,79] Ab initio methods make use of the first principle calculations, they start from the fundamental laws of physics without any assumptions or parameters. These methods are computationally demanding, but they can give accurate results for systems with complex electronic structures. [80,81]

Density functional theory (DFT) is another powerful computational method used to study the electronic structure of molecules and materials. It is a widely used method in theoretical chemistry, materials science, and condensed matter physics. DFT calculations can be used to predict the properties of molecules and materials, such as their structure, stability, and reactivity. In DFT, the electronic structure of a system is described by electron density, which is a function of the positions of the nuclei and the electrons. The electron density is used to calculate the total energy of the system, and this energy can be minimized to predict the ground state structure of the system, but it can be used as well to study the excited state. Therefore, validating the predictions made by DFT calculations against experimental data is also necessary. [82–87]

2 Objectives

The main objective of the thesis was the investigation of the 3D scaffold creation of polysuccinimide-based fibrous scaffolds that can be used later on in tissue engineering. My focus was oriented to experimental research covering the creation of the fibers and to computational simulation to understand the fundamental interactions in the solutions.

Thus, my aim was to produce two-dimensional (2D) and three-dimensional (3D) poly succinimide-based fibrous scaffolds with different salt components and investigate their interaction with the polymer and the solution.

The objectives of the thesis were the following:

1, To investigate the DMF-water systems with computational simulation to understand the solvent effect in the electrospinning system. For that, MD simulation was performed, and analysis was conducted with RDF, NN, VP

2, To investigate the DMF-salt interaction, which can predict the 3D formation during the electrospinning phenomena with DFT calculation and vibrational spectroscopy.

3, To create 3D fibrous scaffolds with electrospinning setups in the presence of different salts for potential tissue engineering applications.

3 Materials and methods

3.1. Density functional theory (DFT) calculation

The optimized configurations of ions and DMF complexes were obtained in a polar medium treated via an implicit solvent approach. As dispersion plays a vital role in describing the interionic and ions-DMF interactions, the M06-2X functional was used to better consider the medium-range dispersion effect. This functional was coupled with 6-311+g(d,p) basis set. [88]

The geometry optimizations were followed by harmonic frequency analysis to ensure that the obtained structure was true minima by the absence of imaginary wavenumber and to rationalize the experimental results regarding the obtained optimized configurations.

Density functional theory calculations were conducted using Gaussian 16 software package then visualization and analysis were performed with Gaussview 6. [89] The calculations were run on the Zeus cluster of the University of Lille HPC center.

3.2. Molecular Dynamics (MD) calculation analysis

Molecular dynamics simulations were conducted on DMF-water mixtures of 11 different compositions and on the two pure liquid forms. The simulation parameters were on canonical (N,V,T) ensemble at a temperature of 298.15K. The concentration of DMF increased by 0.1 steps from neat water ($x_{DMF} = 0$) to neat DMF ($x_{DMF} = 1$) in the systems. In every case, 500 molecules were inserted into a cubic basic box. The length of the edges has been defined with a preliminary, 5 ns long isothermal-isobaric (N,p,T) ensemble simulation, preceded by 10 ns equilibration. The used simulation package was GROMACS 5.1.5. Before starting each simulation, the system's energy has been minimized using the steepest descent algorithm. To maintain a constant temperature, the velocity-rescaling thermostat was used with a relaxation time of 0.1 ps. In the case of (N,p,T) ensemble runs, the Parrinello-Rahman barostat was used to set the pressure of the system to 1 bar with a relaxation time of 0.5 ps.

The MD simulations were performed by Volodymyr Koverga, and I analyzed the provided calculation data of DMF-water with Radial Distribution Function (RDF), Nearest Neighbor Contributions (NN), and Voronoi Analysis methods. The RDF and the

NN were calculated using TRAVIS-1.14.0 software. All the results of the methods were then curve fitted with Gaussian function and deconvoluted with a python software written by me. The results were then collected and plotted with ORIGIN Pro 9.5.1 software.

The RDF is a function of the distance between pairs of atoms or molecules, and it provides information about the probability of finding an atom or molecule at a certain distance from another atom or molecule. The RDF can be used to study the short-range order in a system, such as the arrangements of atoms in a crystal or the density of molecules in a liquid. It can also be used to study the long-range order in a system, such as the periodicity of a crystal. The RDF can be calculated from various types of simulations. [90–93]

The radial distribution of atom *j* around atom *i* can be given as:

$$g_{ij}(r) = \frac{\rho_j(r)}{\rho_j} = \frac{< n_{ij}(r) >}{4\pi r^2 \rho_j \mathrm{d}r} \tag{1}$$

where $\rho_{ij}(r)$ and $<n_{ij}(r)>$ stands for the density and average number of *j* atoms around a reference *i* atom, respectively, in the distance range between *r* and *r*+*dr* from this reference atom, and ρ_j is the overall density of the *j* atoms in the system.

Nearest neighbor method is used to study the local environment of atoms or molecules in a system. The technique involves identifying the closest atoms or molecules to a specific atom or molecule and analyzing their interactions and properties. This approach can give researchers an understanding of the structural, electronic, and thermodynamic characteristics of the system. The contribution of the *k*th nearest neighbor of type *j* around atom *i* to the $g_{ij}(r)$ radial distribution function, $g_{ij}^{(k)}(r)$, can be given as

$$g_{ij}^{(k)}(r) = \frac{\rho_j^{(k)}(r)}{\rho_j} , \tag{2}$$

where $\rho_j^{(k)}(r)$ is the density of the *k*th closest neighbor of type *j* at the distance between *r* and *r*+*dr* from atom *i*. [93–95]

The Voronoi polyhedra method is a technique that is used to evaluate the local surroundings of atoms or molecules in a system. This method is based on the Voronoi

tessellation which partitions space into a set of polyhedra cells, each cell surrounds a specific atom or molecule. The shapes, sizes, and orientations of these polyhedra cells provide information about the coordination of the central atom or molecule and its interactions with its neighbors. This method can be applied to various types of systems, including crystals, liquids, and biomolecules and can be used to evaluate both experimental and computational data to study the structural, electronic, and thermodynamic properties of materials. It is particularly useful in identifying defects, impurities, and interfaces in a material and in understanding the behavior of chemical reactions. [93,96–98]

3.3. Reagents

L-Aspartic Acid (reagent grade ≥ 98 %, Mw ~133, Sigma Aldrich, USA), Orthophosphoric Acid (reagent grade ≥ 99 %, Mw ~98, Sigma Aldrich, USA), N,N-Dimethylformamide (reagent grade ≥ 99.8%, AnalaR NORMAPUR®, VWR Chemicals BDH®, VWR International, USA), $MgCl_2$ (≥ 99 %, Reanal), $CaCl_2$ (≥ 99 %, Reanal), LiBr (≥ 99 %, Acros Organics), NaBr (≥ 99 %, Sigma-Aldrich), NaI (≥ 99 %, VWR), KI (≥ 99 %, VWR), KBr (≥ 99 %, VWR), LiCl (≥ 99 %, Sigma-Aldrich).

3.4. Synthesis of Polysuccinimide

Polysuccinimide (PSI) was synthesized with the equipment shown below (Figure 3.1). The equipment consists of an IKA RV21 rotary evaporator with an IKA HB21 digital heat tank and a Vacuubrand PC3001 VARIO vacuum generator. The evaporator has a thermostat set to -10 ∘C and a KOH trap. After carefully mixing 20g L-aspartic acid and 20g crystalline phosphoric acid, the mixture was added to a pear shape flask (1L) and heated to 180 ∘C under vacuum (3mBar). By the end of a 7-hour-long reaction, one can observe a yellowish-brownish foam-like structure.

When it was cooled down properly, 200 ml dimethylformamide was added and stirred for complete solvation. To remove the unreacted materials, washing, and filtering are necessary. 1600ml distilled water was added and stirred for 10 minutes, then with a G3 type glass filter, the mixture was filtered. The washing and filtering steps were repeated about 3-4 times until the pH was neutral. After that, the PSI powder was dried at 40 C for three days in a dehydrator. The final product had a white color.

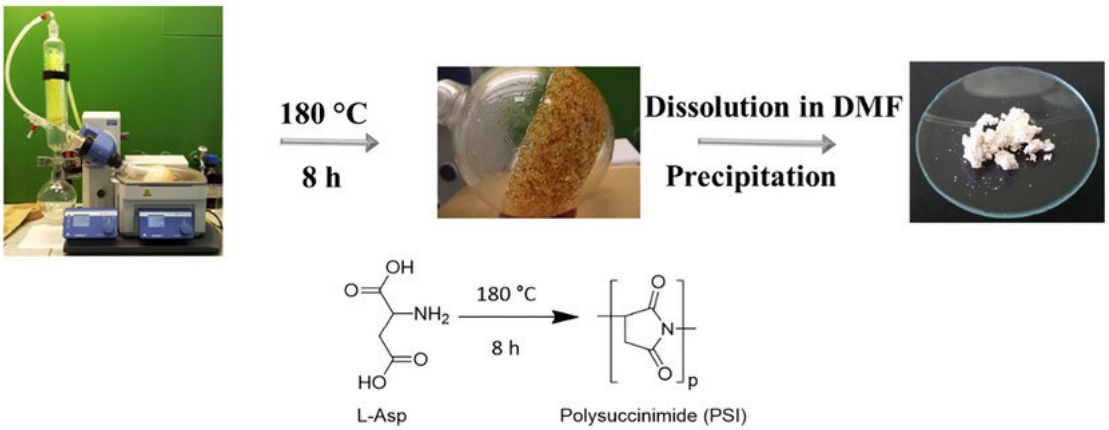

Figure 3.1 Synthesizing and cleaning PSI [46]

3.5. Preparation of solutions

After weighing, the anhydrous salts were dissolved in DMF, stirring on a magnetic stirrer for 8 hours. However, they could absorb water from the air during sample preparation The polysuccinimide was added to the salt-solvent solution to have a 25 w/w% polymer solution and then further stirred for 12 hours. All the solutions prepared for the experiments can be found in Table 1 Solutions for electrospinning, conductivity, and spectroscopy measurements. The solutions in the green-colored cells were used to mix with PSI and electrospun.

Table 1 Solutions for electrospinning, conductivity, and spectroscopy measurements. The solutions in the green-colored cells were used to mix with PSI and electrospun, the samples in the blue text cells were also used for SEM and FT-RAMAN measurements.

	LiCl	**$MgCl_2$**	**$CaCl_2$**	**LiBr**	**NaBr**	**NaI**	**KI**
	w/w%	w/w%	w/w%	w/w%	w/w%	w/w%	w/w%
Conductivity	1	1	1	1	1	1	1
	3	3	3	3	3	3	3
	5	5	5	5	5	5	5
Solubility range, Vibration spectroscopy(Salt-DMF)	1	1	1	1	1	1	1
	2	2	2	2	2	2	2
	3	3	3	3	3	3	3
	4	4	4	4	4	4	4
	5	5	5	5	5	5	5
	6	6		6	6	6	6
	7	7		7		7	7
	8	8		8		8	8
		9				9	9
		10				10	10

3.6. The conductivity of Polymer solutions

The conductivity of the different solutions was measured using a Thermo Scientific Orion 4-Star pH and conductivity meter with a Thermo Orion 013605MD conductivity cell. Calibration points were chosen to have the measured conductivity in between those points. For the measurement, anhydrous $CaCl_2$, $MgCl_2$, LiCl, LiBr, NaBr, NaI, and KI powders were dissolved in DMF at 1, 3, and 5 w/w% concentrations.

3.7. Electrospinning setup

The electrospinning apparat consisted of a Genvolt 73030P power supply, a KD Scientific KDS100 pump, a Fortuna Optima 7.140-33 type syringe, and a Hamilton G18 blunt-end steel needle (Figure 3.2). The collector was a 3D-printed disc of 2 cm diameter, and the distance between the needle and the collector was kept at 10 cm in all cases.

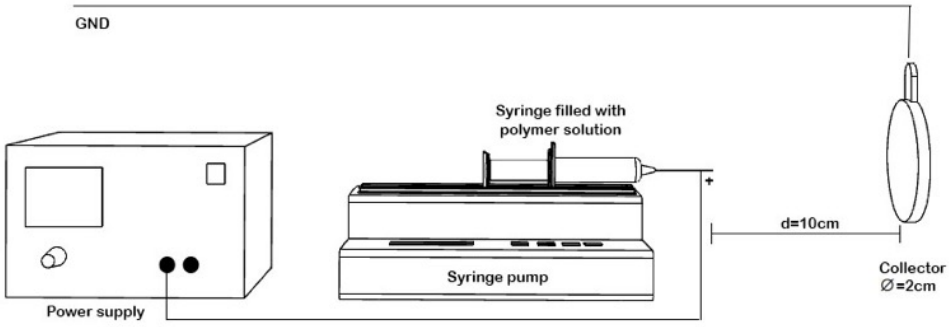

Figure 3.2 Schematic of the electrospinning apparat [24]

Throughout the electrospinning process, the needle was connected to the positive plug of the power supply, and the ground plug was connected to the collector. When the voltage was applied instantly, a small drop of the polymer was pumped out from the needle to start the electrospinning. The flow rate was set to 1 mL/h, the volume of the polymer solution was 1ml, and the applied voltage was 15 kV in all cases.

3.8. Scanning Electron Microscope (SEM)

From the nanofiber mesh samples, pictures were recorded with a JEOL JSM 6380LA SEM device in the Polymer Technology Department of the Mechanical Engineering Faculty of Budapest University of Technology and Economics. The golden coating was applied to the sample with a JEOL JFC-1200 Sputter Coating System. The accelerating voltage was 10 kV, and the magnification was chosen to be 1000x, 2500x,

and 5000x. After electrospinning, samples were collected from three different areas to record pictures from.

The average fiber diameter was analyzed with the Fiji program, and at least 100 fiber diameters were measured from each area at the same magnification. To avoid charge accumulation, silver colloid paint was applied on the edges of the sample. Two-sample Student t-tests were conducted using the averages and standard deviations of the samples to compare the averages double-sided. It was assumed that the fiber diameter showed a normal distribution.

3.9. Fourier transform infrared spectroscopy (FTIR)

FTIR method is primarily used for qualitative measurements. The ATR-FTIR spectra were recorded on the fiber meshes using a JASCO 4700A (JASCO Ltd., ATR Pro ONE) instrument, and the evaluation was performed using the SpectraAnalysis program.

A diamond probe head containing a 1.8 mm spherical diamond crystal was used for the measurements, and a DTGS detector was employed during the experiments. 128 parallel measurements were performed for each sample, averaged over the spectra obtained. The spectra of the pure diamond crystal and the saturated water vapor were subtracted from the spectra of the samples. In all cases, the wavenumber detection range was 4000 and 400 cm^{-1} with a resolution of $2cm^{-1}$.

ATR-FTIR spectra of the different salt solutions (Table 1were recorded on a BRUKER Vertex 70V FT-IR instrument. The spectra were acquired, and the baseline was corrected using OPUS 7.5 software and evaluated using Spectragryph 1.2.10 software. [99] For each sample, 64 measurements were performed, detecting between 5000 and 600 cm^{-1} with a resolution of $2cm^{-1}$. Deconvolution of the observed peaks was carried out with Microsoft Excel and its built-in Solver plugin. (Figure 3.3) Gaussian curves were fitted for the peaks and Lorentzian where shoulders appeared. After an initial guess, the solver plugin tries to calculate the best fit. With this process, one can have information of the peak's height, position, width and the Chi-square.

Height	0,1531104	1,6035289	0,1650087				Chi sq sum
Center	1628,0611	1659,6778	1685,3389				0,0115231
Width	8,4653337	13,618735	7,9159311	30			

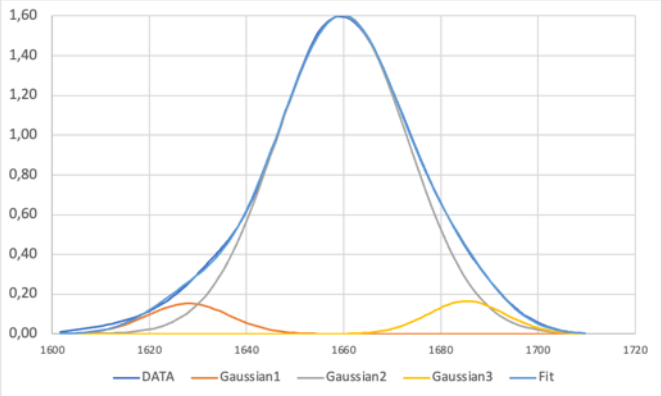

Figure 3.3. An example of the fitting process in the case of $CaCl_2$ 2w/w%

3.10. FT-Raman spectroscopy

FT Raman spectrometry is a complementary spectroscopic method of infrared spectroscopy. Both investigate the molecular motions of matter, but the sensitivity of each method is different for specific functional groups.

The measurements were performed with a Bruker RFS 100/S FT-Raman instrument. Before the measurement, the detector was cooled with liquid nitrogen and allowed to stabilize for 1 hour. The powdered samples (PSI, LiCl, $MgCl_2$, and $CaCl_2$ powders) and polymer meshes (Table 1) were compressed in a sample holder of a measuring cell before the measurement. The laser beam was focused on the sample surface to achieve maximum intensity, and the laser power was chosen to be 50mW. The resolution was 2 cm^{-1}, and the recorded range was 100-4000 cm^{-1}. To optimize the signal-to-noise ratio, samples were generally measured in 14000 to 22000 replicates. Measurements and baseline correction were performed using OPUS 6.5 software, and evaluations were performed using Spectragryph 1.2.10 software.

4 Results

In the process of electrospinning, the polysuccinimide-based three-dimensional nanofibers are mixed with salts, DMF and the unavoidable water moisture. Indeed, the presence of water in the salts' water-binding capability and humidity cannot be ignored, as it is assumed that this also a cause of the 3D formation. In order to characterize the local structure in DMF-water mixture MD simulations were conducted. The salt and DMF mixtures affect in an indirect way the quality, the diameter and the surface roughness of the electrospun fibers. Therefore, vibrational spectroscopy and DFT calculations were combined to investigate the local structure of the DMF and salt mixtures.

4.1. Analysis of DMF-Water mixture simulations

In the following part of my thesis, I will summarize the results about the mixture dependence of the local structure in DMF-water mixture, that were obtained using molecular dynamics simulations. To achieve this goal the statistical observables such as the radial distributions functions, the nearest neighbor radial distribution as well the metric distributions (such as volume, asphericity, vertex radius) of the Voronoi polyhedra were calculated and their dependence on the mixture composition were analyzed.

4.1.1 Water- water correlations

The molecular dynamics simulation results were analyzed first with radial distribution function (RDF) method. The radial distribution function (RDF) is a statistical tool to define the spatial distribution of particles in a system. With its help, one can describe the probability of finding a particle at a certain distance from another particle, given the number density of particles in the system. It can be used to study the structure and dynamics of materials at the atomic and molecular levels. It is often obtained by averaging over a large number of configurations and is plotted as a function of distance and typically normalized by the number density of particles in the system.

Figure 4.1a shows RDF of O and H atoms, $g_{O_wH_w}(r)$. Pure water has two distinct peaks, one is at 1.9 Å corresponding to the H-bonding O-H pairs and another one is at 3.2 Å related to the non-H bonding atom pairs of an H-bonded pair of water molecules. One can observe, the height of the two peaks systematically increases as DMF concentration is increases. A minimum can be observed at 4.2 Å and a third peak is

starting to evolve around 7.4 Å as the concentration of DMF increases. In the inset the running coordination number of Hw around Ow can be observed, $c_{\mathrm{O_wH_w}}(r)$.

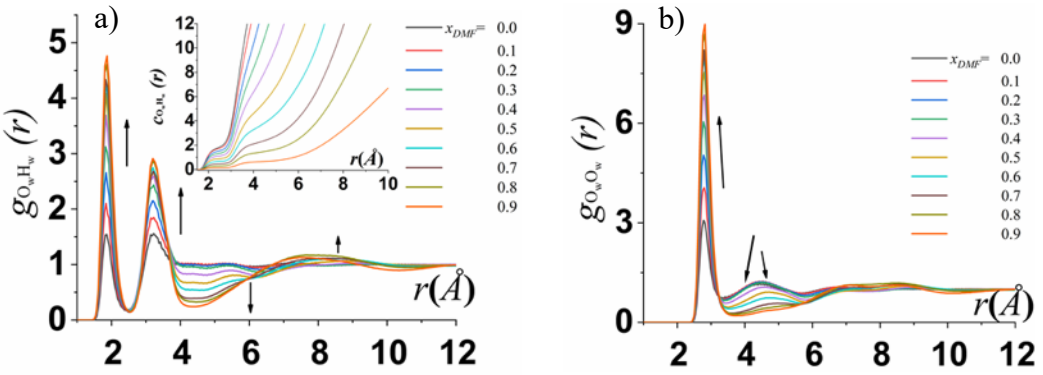

Figure 4.1 The radial distribution function for (a) the O and H atoms in water, and (b) only for the O atoms in water. The inset displays the running coordination number of the Hw atoms surrounding the Ow atoms in these systems. The arrows indicate how these functions change as the DMF mole fraction increases. [93]

Figure 4.1b shows the RDF of O and O atoms where the enhanced H-bonding is also present. The height of the first peak corresponding to the H-bonded pairs increases as the concentration of DMF increases. One can observe that also the minimum emerges at 3.3 Å. This demonstrates the gradual disappearance of the interstitial water neighbors.

To deconvolute the radial distribution function, the first five H_w neighbors of the water O atoms were analyzed with the function $g^{(k)}_{\mathrm{O_wH_w}}(r)$ where $k = 1,2,3,4,$ and 5, where k denotes the neighbors. The results are shown in Figure 4.2.

In the case of k = 1, neat water has only one observable peak at 1.9 Å which will also dominate the k = 2 function. When observing k = 3, it is observable as a shoulder which evolves to a peak at 3 Å while becoming the dominant peak of the function and contributing to the second peak of the total RDF. For the k = 4 and 5 neighbors, it is also remains to be the dominant feature.

In the case of the first neighbor, when increasing the concentration of DMF, another peak is evolving at 3 Å. When reaching 0.8 mole fraction of DMF, a third peak also emerges between 5 and 6 Å, which becomes broader and shifts farther.

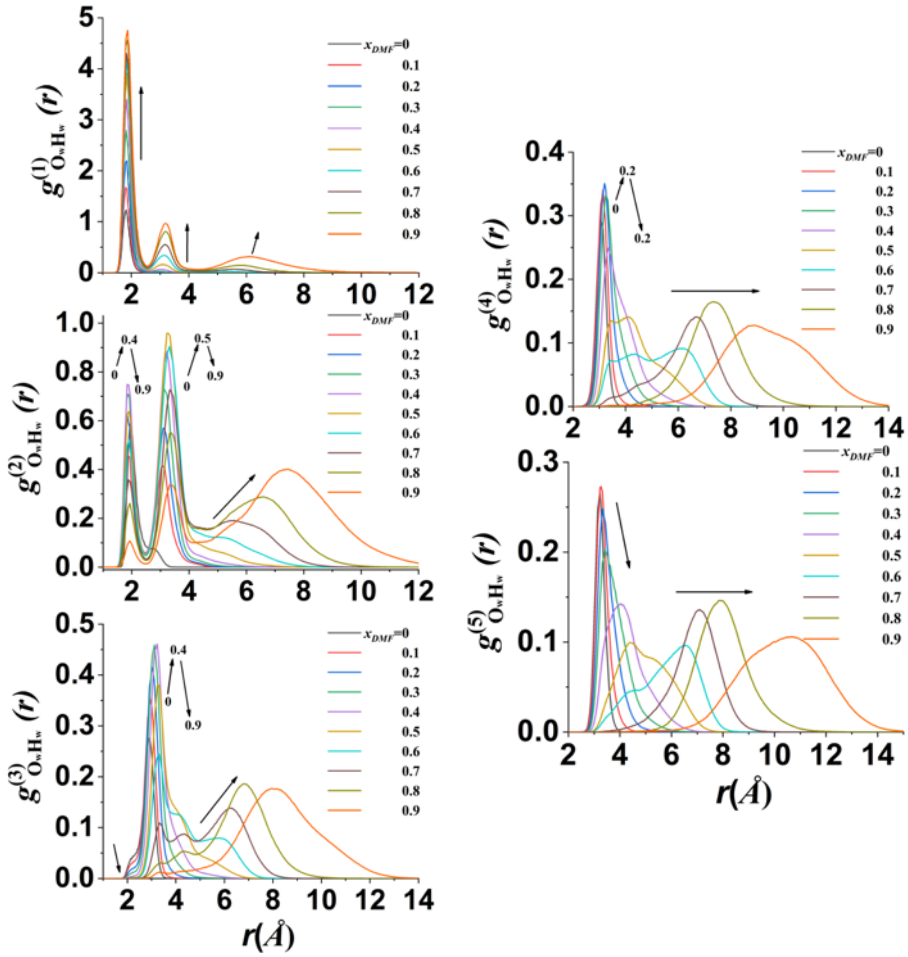

Figure 4.2 Contribution of the first five nearest neighbors (from g(1) to g(5)) to the $g_{O_wH_w}(r)$ radial distribution function. The arrows indicate how these functions change as the DMF mole fraction increases. [93]

4.1.2 Gaussian curve fitting

To quantify the RDF results, Gaussian functions were fitted to the individual peaks of $g^{(k)}_{O_wH_w}(r)$. From the Gaussian fits the position, width, and intensity (height) are presented in Figure 4.3 a-e for the *k* values of 1-5, respectively.

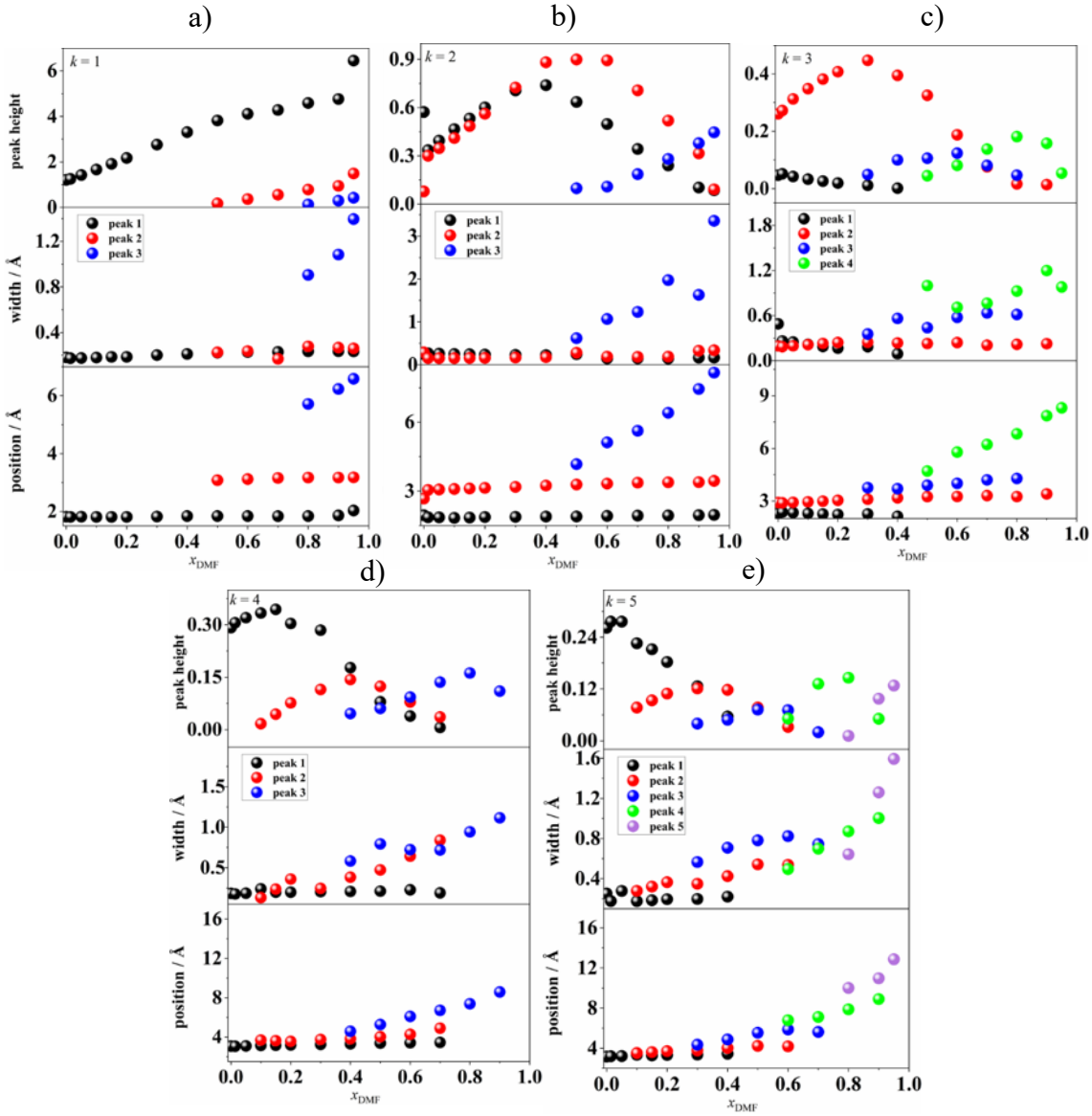

Figure 4.3 Gaussian functions fitted to the individual peaks of the contributions of (a) the first, (b) second, (c) third, (d) fourth, and (e) fifth nearest H_w neighbors of the O_w atoms to the radial distribution function. [93]

From Figure 4.3 one can observe that both the position and width of the first two peaks which are corresponding to the H-bonded water pairs are constant all the way, while the third peak increases gradually while increasing the DMF content. The second neighbor contribution has a very similar trend, only the third peak appears at a lower, 0.5 mole fraction. Also, that the heights of the first two peaks reaches a maximum in the 0.3 -0.6 mole fraction range.

4.1.3 Water-DMF and Water-Water relations

When observing the mixtures of water and DMF one would expect a competition between the O atoms for the H atoms of water. In Figure 4.4 one can observe the RDF of the DMF O and water H atoms of the different compositions. The results are very similar to the Ow-Hw function. With increasing DMF mole fraction, the height of the first two peaks increases as well, while a second minimum and a third peak evolves. Similarly, to the water-water H-bonds, DMF-water H-bonds also persist even at very low water mole fractions.

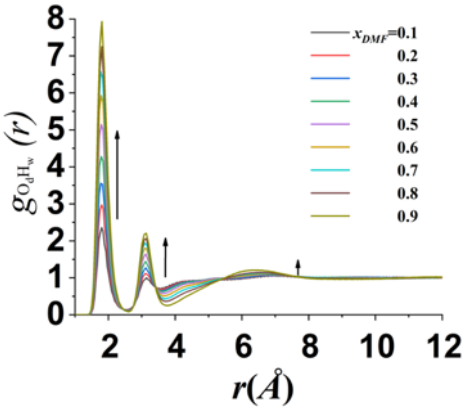

Figure 4.4 Radial distribution function of the DMF O and water H atoms. The arrows indicate how these functions change as the DMF mole fraction increases. [93]

The RDF deconvolutions also show similar results than in the case of the Ow-Hw function (Figure 4.5). Thus, for the first neighbor, the height of the first peak increases with increasing DMF content, while for the second neighbor it has a maximum. For the third neighbor, the first peak evolves to be the second peak of the total RDF. Due to various DMF-water pairs bridges several peaks occurring between 4 and 8 Å.

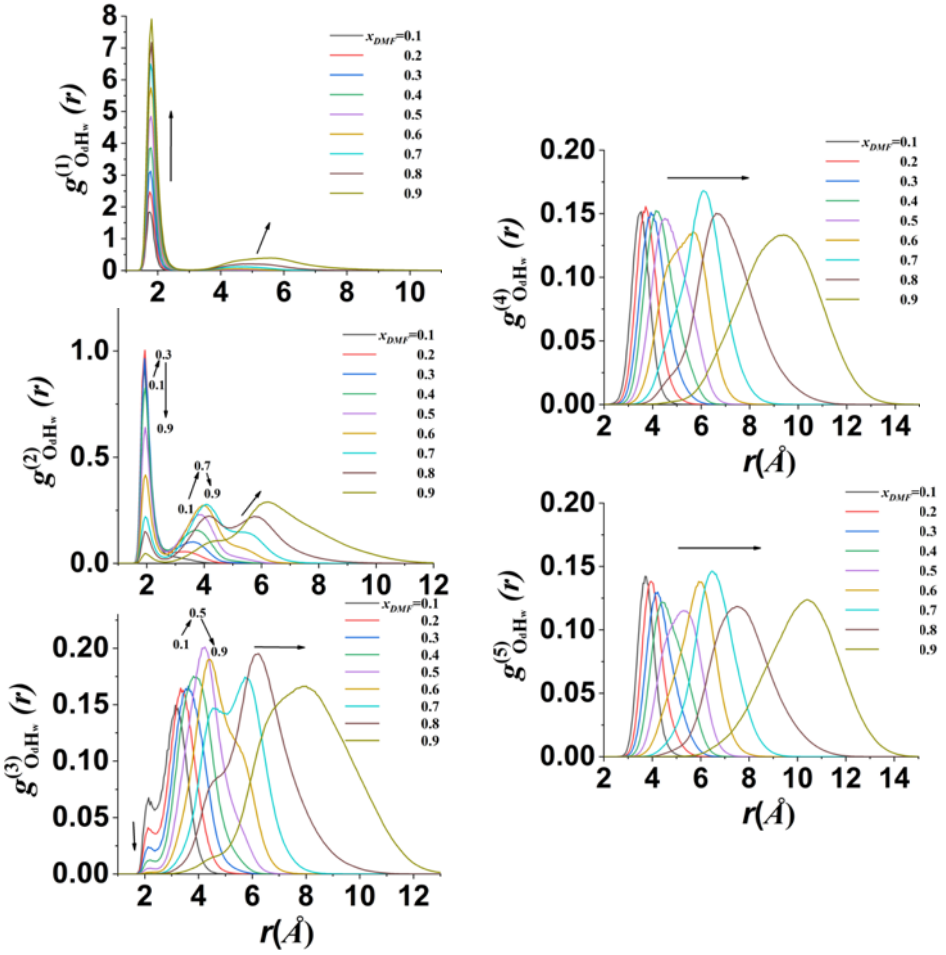

Figure 4.5 RDF of the first five nearest neighbors. The arrows indicate the evolution of these functions with increasing DMF mole fraction. [93]

The RDF of the DMF O and H atoms (Figure 4.6). and also its first five neighbor deconvolution (Figure 4.7) shows a very different behavior from the other two shown before. The RDF of pure DMF shows two distinct peaks, one is corresponding to the nearest Od-Hd neighbor and the other molecules in the first coordination shell. One is observed at 2.5 Å and the other is at 6.3 Å.

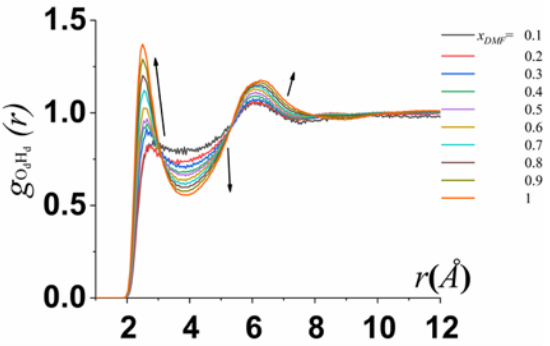

Figure 4.6 Radial distribution function of the DMF O and H atoms. The arrows indicate how these functions change as the DMF mole fraction increases. [93]

The first peak can be observed at 2.5 Å and indicates the presence of weak, C-H….O type H bonds. [100] Interestingly while decreasing DMF content, the height of the peak also decreases contrary to what can be observed at $g_{O_wH_w}(r)$.

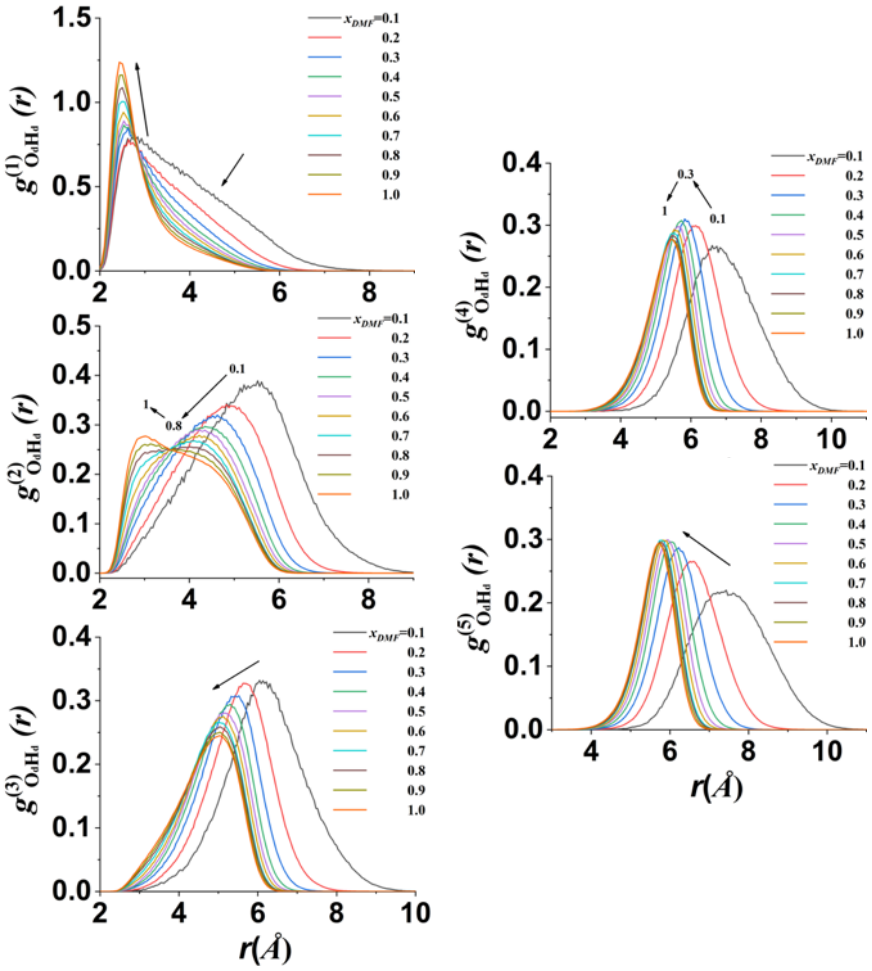

Figure 4.7 The first five nearest neighbors of the radial distribution function. The arrows indicate the evolution of these functions with increasing DMF mole fraction. [93]

The second peak is at 6.3 Å also decreases with decreasing DMF content. However, this decrease is rather weak above x_{DMF} = 0.5, and gets significantly stronger in more dilute systems. In the case of the other convolutions, they are shifted to larger distances, and gets stronger below the x_{DMF} value of about 0.3-0.5.

To quantify the number of water-water and water-DMF hydrogen bonds in the system as a function of composition, I calculated the average number of hydrogen bonds (n_{HB}) formed by two water molecules and by a water and a DMF molecule in the entire system at each composition considered. (Figure 4.8)

It is considered that two molecules form a hydrogen bond if their oxygen atoms are closer to each other than 3.5 Å and the bonding hydrogen atom is closer to the accepting oxygen atom than 2.45 Å (these cutoff values being the first minimum positions of the corresponding radial distribution functions).

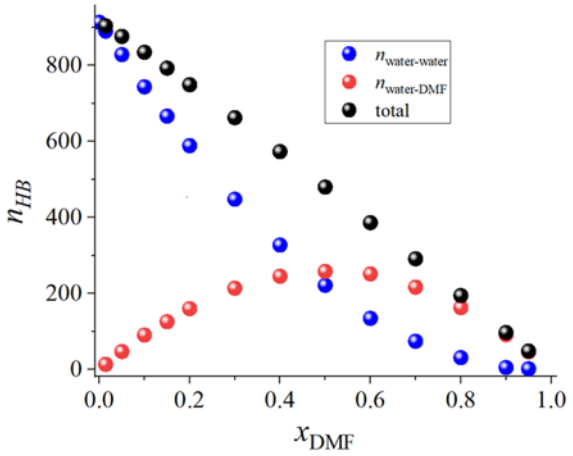

Figure 4.8 Average number of hydrogen bonds in ● water-water-, ● water-DMF mixtures and the ● total number [93]

4.1.4 Voronoi polyhedra analysis

The distribution of the Voronoi polyhedra of the molecules (P(V), only water (Pw(V) and only DMF molecules ($P_D(V)$ can be observed in Figure 4.9 The distribution of Voronoi polyhedra volume surrounding molecules in systems of various compositions, (a) considering all molecules, (b) only DMF molecules, and (c) only water molecules. The insets shows the same data on a logarithmic scale. The arrows depict the changes in these distributions as the DMF mole fraction increases. . In the case of P(V) the distribution exhibits a smooth shift between pure water and pure DMF as the system composition changes. The difference in peak positions between the two clean solutions merely reflects the fact that liquid water has a much higher molecular number density than DMF. When adding a component to the other, a tail is appearing on the corresponding side of the distribution. While increasing the concentration, the tail turns into a shoulder and then it'll become a second peak. The two peaks reach an equal height at 0.4 mole fraction. Accordingly, the main peak shifts to larger V values when the system is water-rich, and to smaller values when DMF is dominant.

When analyzing Pw(V) and $P_D(V)$ one can get a better understanding of the individual component behavior. When decreasing the concentration of the observed

component, the distinct peaks progressively shift to larger V values while broadening, matching the effect of dilution. Most important feature of the distributions is that they are not developing a long tail of exponential decay when decreasing the concentration, which means the system lacks microheterogeneities. Yet, at larger concentrations the peak changes quite slowly, which means that the major component still has a significant portion which behaves similarly that in the case of pure liquid.

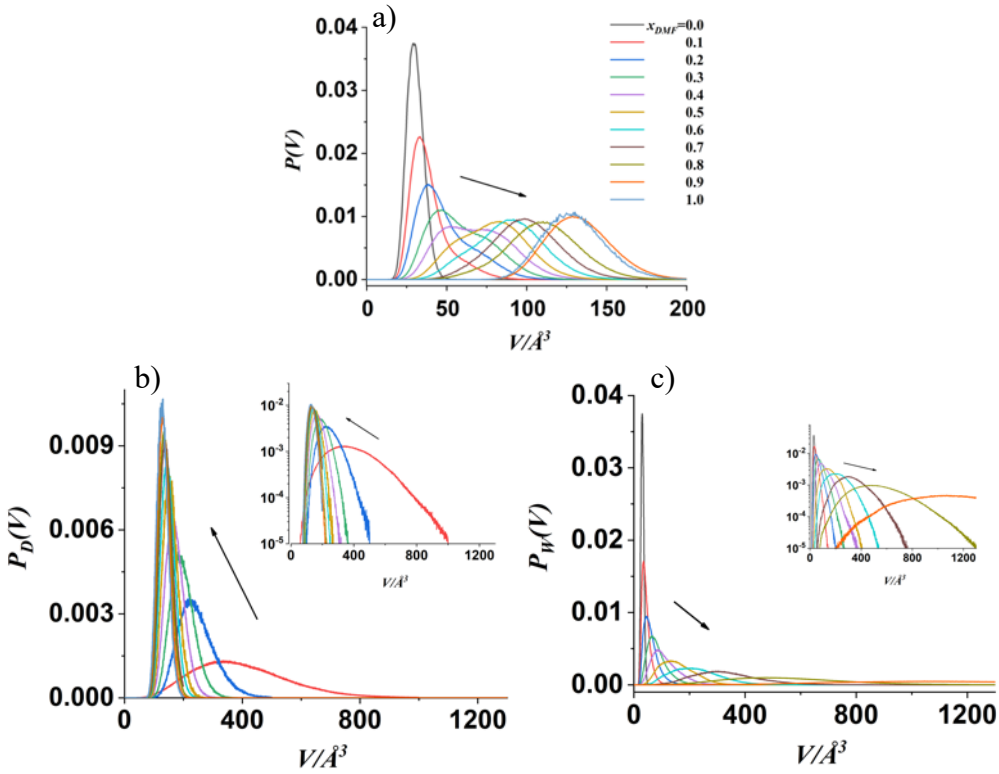

Figure 4.9 The distribution of Voronoi polyhedra volume surrounding molecules in systems of various compositions, (a) considering all molecules, (b) only DMF molecules, and (c) only water molecules. The insets shows the same data on a logarithmic scale. The arrows depict the changes in these distributions as the DMF mole fraction increases. [93]

One can observe a very similar behavior from the void radius distribution. It is a statistical measure of the sizes of the empty spaces within a Voronoi tessellation. It can be calculated by measuring the void radius for each void and plotting the frequency of the different sizes. The distribution can provide insight about the spatial patterns of the data. In Figure 4.10 the result of the analysis for all molecules (P(R)), only water (Pw(R)) only DMF molecules ($P_D(R)$) are plotted. These distributions characterize the local environment of the intermolecular voids rather than that of the molecules themselves.

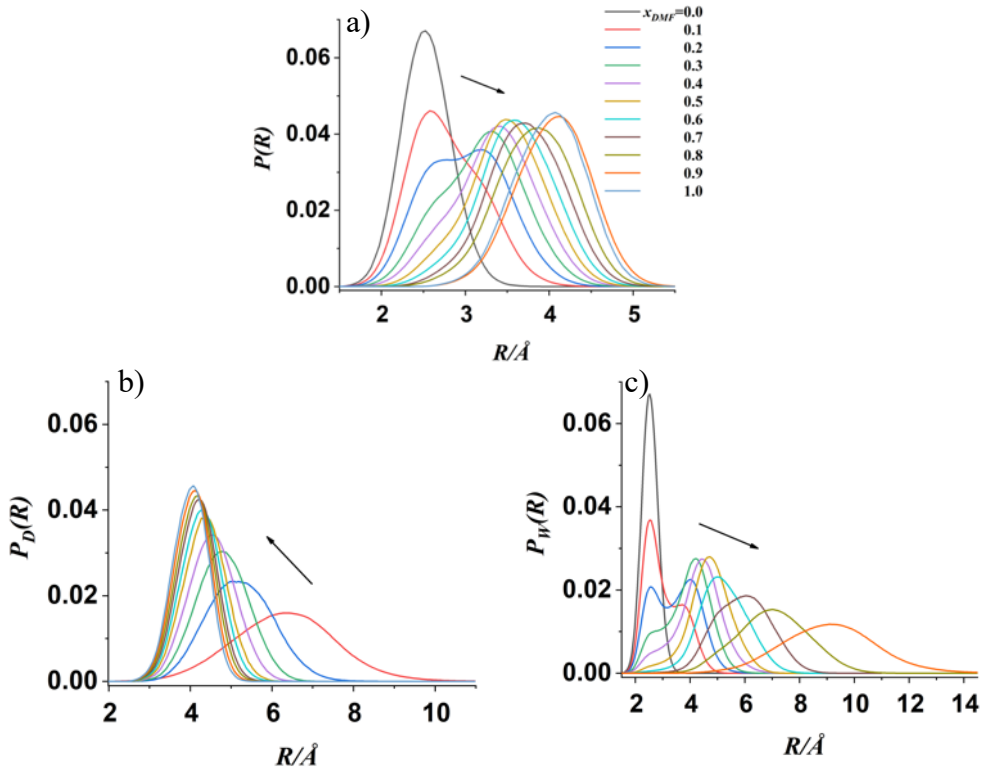

Figure 4.10 The distribution of the radius of the largest spherical voids among molecules in systems of diverse compositions as obtained from Voronoi analysis, considering (a) all molecules, (b) only DMF molecules, and (c) only water molecules. The arrows indicate how these distributions change as the DMF mole fraction increases. [93]

Finally, the behavior of the asphericity parameter distribution, shown in Figure 4.11 The asphericity parameter distribution of Voronoi polyhedra around the molecules in systems of different compositions, as obtained considering (a) all molecules, (b) only the DMF molecules, and (c) only the water molecules. when considering all molecules as well as only the water or only the DMF molecules in the analysis (P(R), Pw(R), and P_D(R), respectively) reinforces the conclusions that were drawn from the analysis of the radial distribution functions. Asphericity refers to the shapes of the Voronoi cells, how much they differ from a perfect sphere. A low value means that a cell is mainly spherical, while a high value means that it is elongated or flattened.

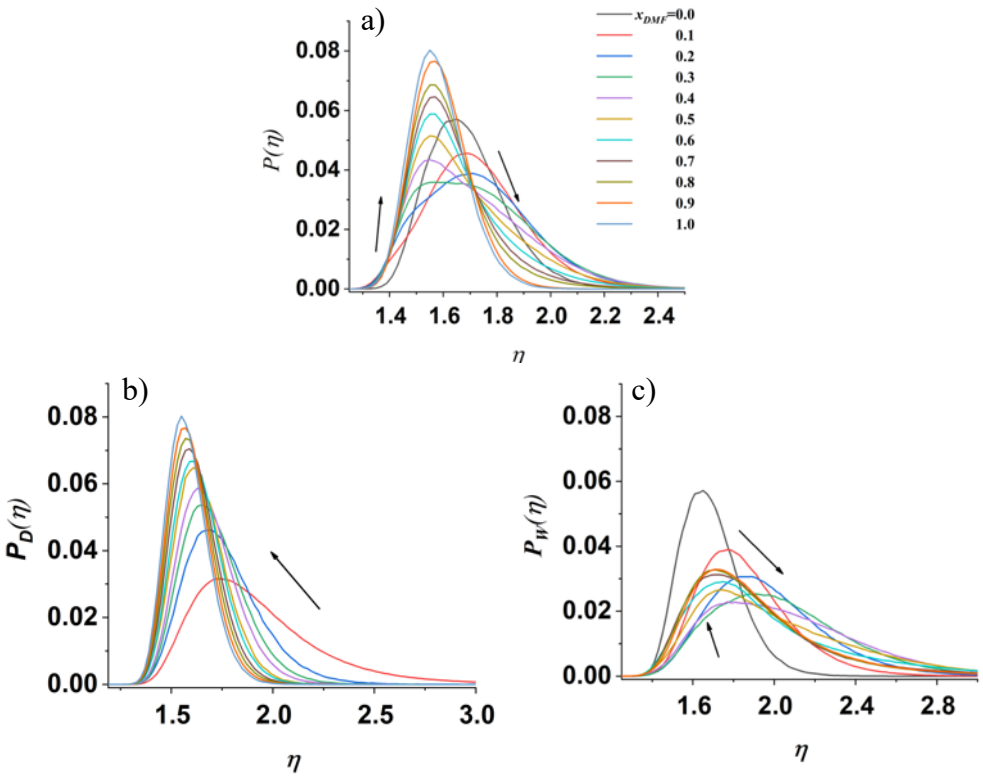

Figure 4.11 The asphericity parameter distribution of Voronoi polyhedra around the molecules in systems of different compositions, as obtained considering (a) all molecules, (b) only the DMF molecules, and (c) only the water molecules. [93]

4.2. Characterization of the salt solutions

After the characterization of the solvent and water mixtures with molecular dynamics simulations, the salt-solvent solutions were analyzed with vibrational spectroscopy and DFT calculations. Indeed, the presence of inorganic salts in different concentrations causes some effect for the 3D structure formation during the electrospinning procedure which is not fully described in the literature yet. Using FTIR spectroscopy and density functional theory calculation (DFT) the effect of the salt in the solvent (dimethylformamide) and the structural changes of the fibrous mesh by macroscopic and SEM (Scanning Electron Microscopy) images were examined.

4.2.1 Solvation of salts in DMF

The selection of salts was based on their solubility in DMF as per the IUPAC Solubility Data Series. A range of solutions were made using various inorganic salts (Table 2).[101]

Table 2 Solutions of inorganic salt – DMF. Green color indicates that the salts are inducing 3D fluffy structure in a reproducible way, on the other hand the blue and grey colors represents where neither the 2D or the 3D structures are reproducible. [24]

Salt name	LiCl	mol/l DMF	$MgCl_2$	mol/l DMF	$CaCl_2$	mol/l DMF	LiBr	NaBr	NaI	KI
Concentration in DMF (w/w%)	1	0.23	1	0.1	1	0.09	1	1	1	1
	2	0.46	2	0.2	2	0.17	3	3	3	3
	4	0.93	3	0.41	3	0.26	5	5	5	5
	5	1.18	4	0.52	4	0.36				
	6	1.43	5	0.64	5	0.45				
	8	1.94	6	0.87						
			10	1.11						

After dissolving the salts completely, the solutions were clear, but in certain cases (such as with KI, NaI, and $MgCl_2$) the colors became darker as the salt concentration increased. In some instances, likely due to external factors, crystals formed when the solubility was lower than expected (Figure 4.12 a) DMF b) LiBr 1-10w/w% c) KI 1-10w/w% d) 10w/w% LiCl 10w/w% crystal growth).

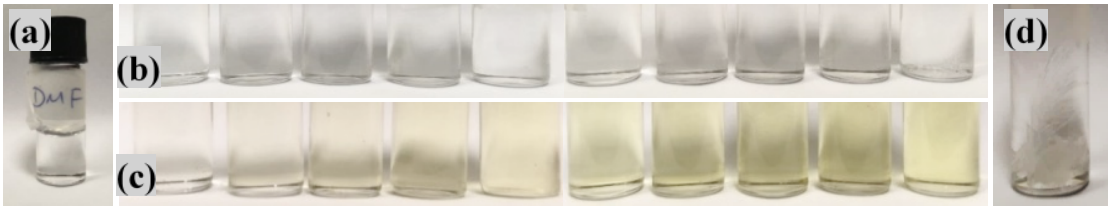

Figure 4.12 a) DMF b) LiBr 1-10w/w% c) KI 1-10w/w% d) 10w/w% LiCl 10w/w% crystal growth [24]

4.2.2 Conductivity of the DMF-salt solutions

Conductivity is a crucial aspect of solutions used in electrospinning, thus it was measured in the DMF-salt solutions. The results are shown in Figure 4.13 . As more ions were added, conductivity gradually increased. The conductivity values depend on the type of ions dissolved, with conductivity being much higher (over 8 mS/cm) for salts containing iodide and bromide anions compared to those with chloride anions.

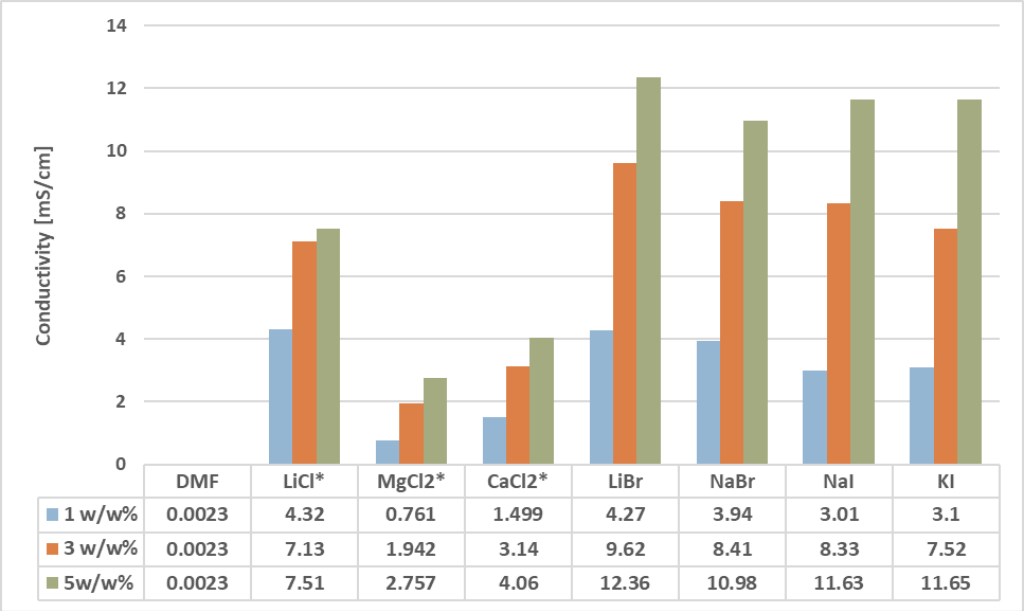

	DMF	LiCl*	MgCl2*	CaCl2*	LiBr	NaBr	NaI	KI
1 w/w%	0.0023	4.32	0.761	1.499	4.27	3.94	3.01	3.1
3 w/w%	0.0023	7.13	1.942	3.14	9.62	8.41	8.33	7.52
5w/w%	0.0023	7.51	2.757	4.06	12.36	10.98	11.63	11.65

Figure 4.13 The conductivities of various salt solutions. The '' symbol denotes the salts that resulted 3D structures during electrospinning.*

4.2.3 Vibrational spectroscopy on DMF-salt solutions

IR measurements were performed on the solutions to detect any signs of interaction between ions and ions, as well as ions and DMF. (Figure 4.14 and Figure 4.15).

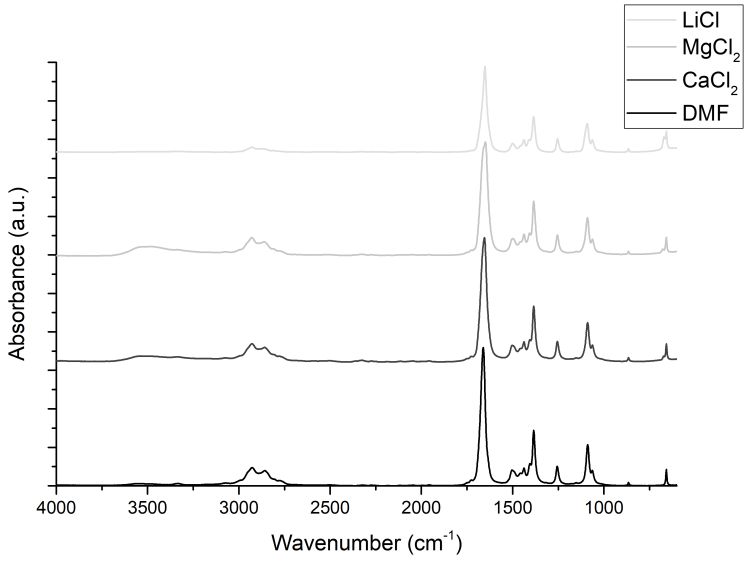

Figure 4.14 The FTIR spectra of the DMF, and the different inorganic salts (LiCl, $MgCl_2$, $CaCl_2$) dissolved in DMF [24]

DMF has two distinct vibrational modes of great interest in my case: one at 1667 cm^{-1}, which is a C=O stretching mode, and another at 661 cm^{-1}, which is a bending

vibrational mode. These peaks can be analyzed to investigate their dependence on the solvation shell of the ions. The results are shown in Figure 4.15a and Figure 4.15b, with the C-H bending vibrational modes also plotted in the inset.

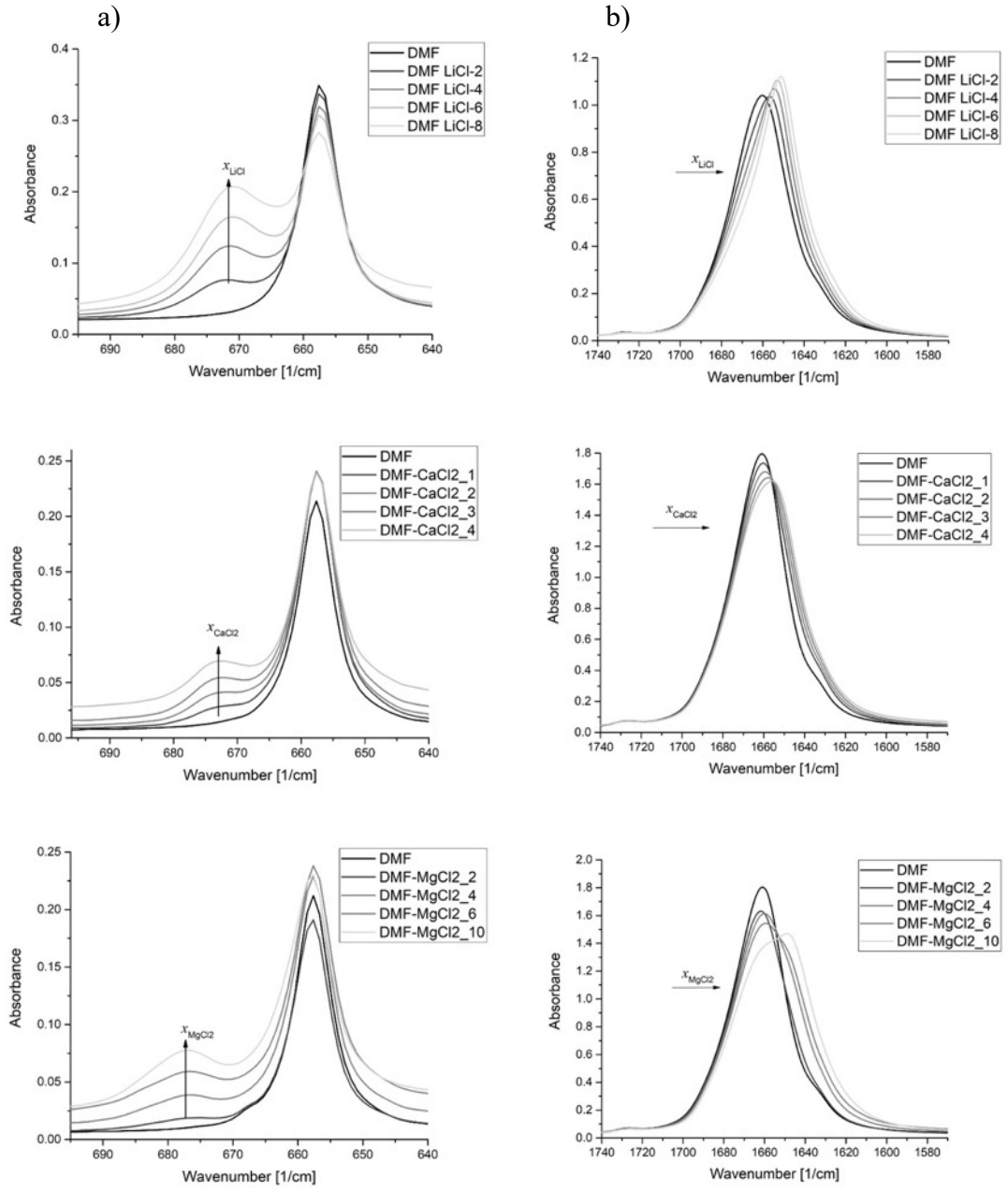

Figure 4.15 IR spectra of the $NC^{H}=O$ a) and the C=O b) vibrational modes in mixtures of LiCl (2, 4, 6 and 8 w/w%) $CaCl_2$ (1, 2, 3 and 4 w/w%) and $MgCl_2$ (2, 4, 6 and 10 w/w%) with DMF. [24]

A new broad spectral feature (appearing as a peak around 675 cm^{-1}) develops gradually as the salt concentration increases, near the $NC^{H}=O$ bending peak (main peak, around 660 cm^{-1}). The highest intensity C=O peak is highly asymmetric and skewed,

which may be attributed to the presence of a spectral contribution at the lower wavenumber side (around 1640 cm^{-1}) when coordinated by Li^{+}, Ca^{2+}, or Mg^{2+}.

4.2.4 Deconvolution of the observed peaks

To measure the modifications in the $NC^{H}=O$ bending mode, the spectral region was fitted with two spectral contributions. The position and intensity ratio are plotted in Figure 4.16a for each salt-DMF mixture. The position of the main peak does not change with the presence of salts, however, the new peak varies depending on the type of salt. A significant shift upwards can be seen in the case of the $MgCl_2$-DMF mixture, indicating that the DMF molecules are strongly bound to $MgCl_2$, more than to LiCl and $CaCl_2$ salts.

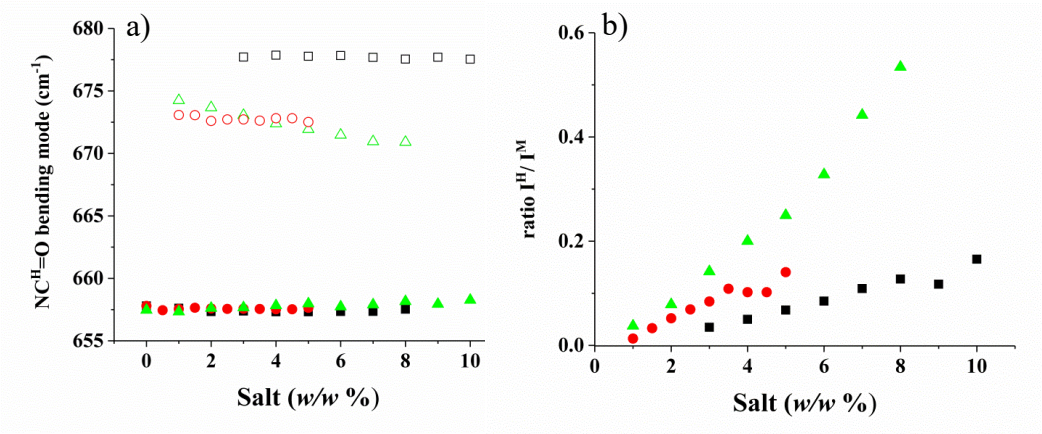

Figure 4.16 (a) The concentration dependence of the position of the higher (new) peak and the main wavenumbers of the $NC^{H}=O$ bending mode. The symbols △ and ▲ are describing the new and the main peak for LiCl mixtures, ○ and ● for $CaCl_2$ and □ and ■ for $MgCl_2$. (b) The concentration dependence of the ratio between the highest wavenumber spectral contribution intensity, I^H, and the main one, I^M. ▲ for LiCl mixtures, ● for $CaCl_2$ and ■ for $MgCl_2$. [24]

4.2.5 Intermolecular interactions between salt-DMF mixture

To gain a deeper understanding of the interactions between salt and molecular solvent mixtures, DFT calculations were carried out. The outcome of the geometry optimization can be seen in Figure 4.17 Optimized geometries for a) 4DMF b) 4DMF - 2LiCl c) 4DMF – $2CaCl_2$ d) 4DMF – $2MgCl_2$. Observed interatomic distances (Å) represented with dotted lines. . Table 3 shows the values of the maximum and minimum intramolecular distances and the frequencies of the C=O, C-H, and $NC^{H}=O$ modes. The intramolecular C=O distances increases, C-N and C-H (of the amide group) distances

decreases in the following order LiCl < $CaCl_2$< $MgCl_2$. The corresponding C=O, C-H wavenumber values increase and NC^{H}=O wavenumber values decrease.

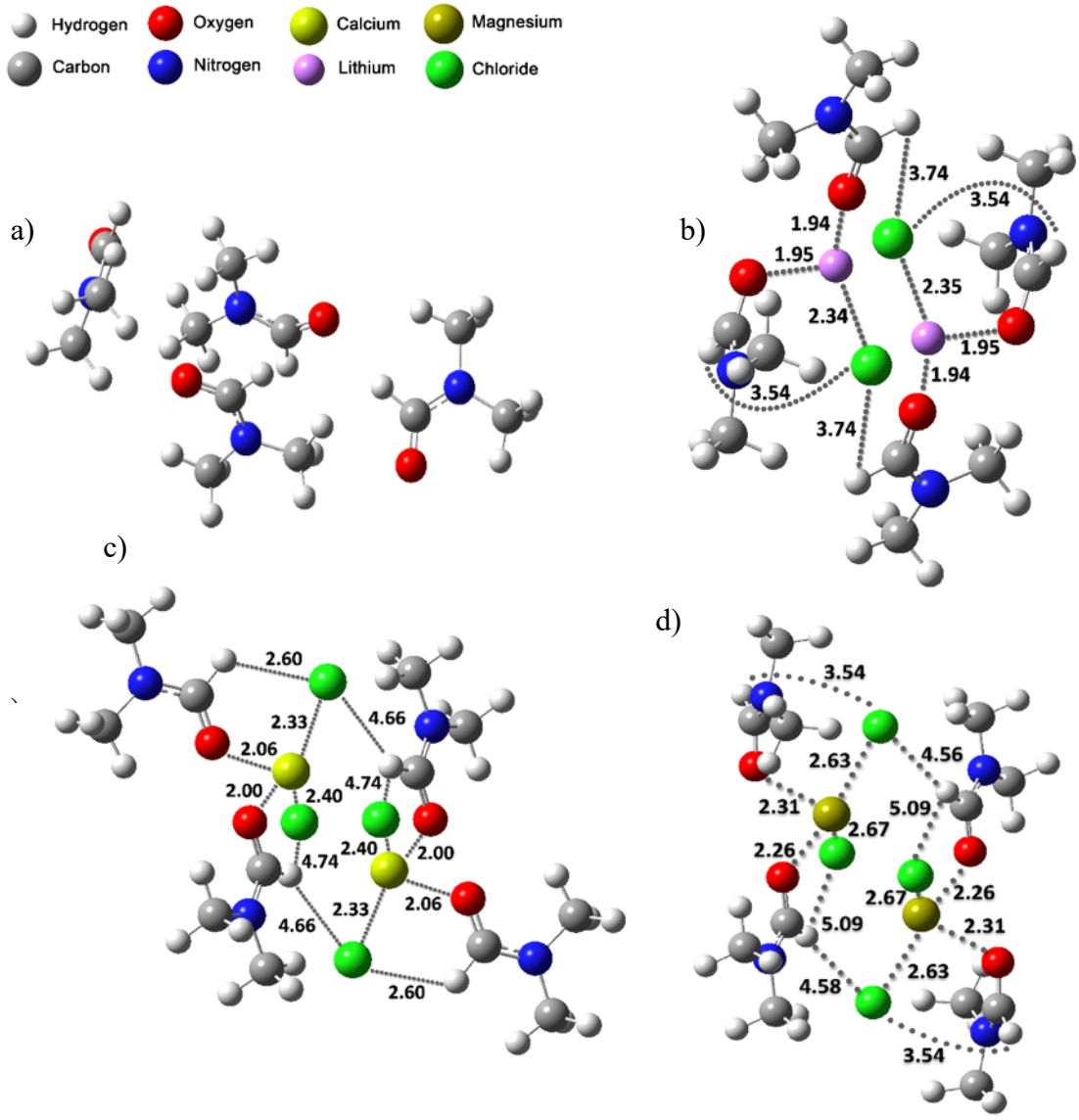

Figure 4.17 Optimized geometries for a) 4DMF b) 4DMF - 2LiCl c) 4DMF – 2$CaCl_2$ d) 4DMF – 2$MgCl_2$. Observed interatomic distances (Å) represented with dotted lines. [24]

Table 3 Intra molecular, inter ions and atoms of DMF as obtained by DFT calculations on the configurations given in Figure 4.17. [24]

Intra molecular												
	max d(C=O) / Å	min d(C=O) / Å	max d(C-N) / Å	min d(C-N) / Å	max d(C-H) / Å	min d(C-H) / Å	max ((ν) (C=O)/ cm-1)	min ((ν) (C=O)/ cm-1)	max (δ(C-H)/ cm-1	min (δ(C-H)/ cm-1)	max (δ(NC^ H=O)/ cm-1)	min (δ(NC^ H=O)/ cm-1)
4DMF	1.222	1.216	1.353	1.349	1.104	1.1	1782	1753	1439	1426	678	670
4DMF-2LiCl	1.228	1.227	1.336	1.336	1.102	1.099	1765	1751	1432	1430	684	681
4DMF-2$CaCl_2$	1.238	1.236	1.329	1.324	1.097	1.097	1747	1733	1428	1427	688	683
4DMF-2$MgCl_2$	1.243	1.231	1.336	1.321	1.096	1.095	1753	1729	1427	1422	705	689

Inter ions –DMF														
4DMF	d(Cation …O) / Å		d(Cation …H-C) / Å		d(Cation …N) / Å		Cation …O=C / deg		d(Cl...O) / Å		d(Cl...H-C) / Å		d(Cl...N) / Å	
4DMF-2LiCl	1.951	1.947	3.591	3.393	3.392	3.33	119	43	3.362	3.317	3.745	3.547	3.35	-
4DMF-2$CaCl_2$	2.318	2.269	3.907	3.894	4.169	3.866	139	44	3.334	3.306	3.547	3.306	3.547	3.478
4DMF-2$MgCl_2$	2.004	2.068	3.551	3.185	4.256	3.776	140	129	3.181	3.14	2.601	3.08	4.538	3.630

The outcome suggests that the cation is closer to the O atom than the anion, while the anion is closer to the N atom than the cation.

4.3. Creating fibrous meshes using electrospinning

Table 1 shows all the different concentrations that were electrospun to determine at which level 3D formation would occur. In Figure 4.18 Planar meshes using KI and KBr, one can see fibrous meshes formed by potassium iodide and potassium bromide that resulted in planar meshes on the collector.

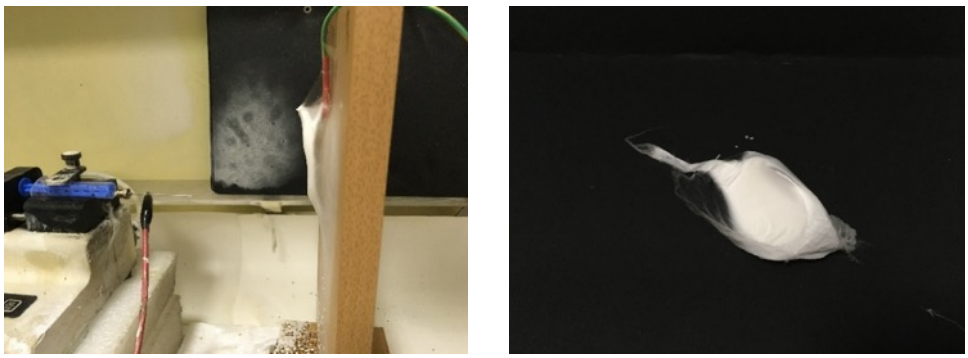

Figure 4.18 Planar meshes using KI and KBr. [24]

Figure 4.19 illustrates a good example of the predicted 3D, sponge-like meshes that were collected when 3w/w% $CaCl_2$ was added to the system. At this concentration, the 3D expansion was the most significant compared to any other compound.

Figure 4.19 Macroscopic view during and after electrospinning of $CaCl_2$ 3w/w% solution. [24]

4.3.1 Fiber characterization with Scanning Electron Microscopy (SEM)

In the left side of Figure 4.20 the representation of some three-dimensional structures can be observed from different salts. The macroscopic shapes vary each time, due to the fact that the charges accumulate differently and there's a huge instability during the flight of the fibers. On the right side, the SEM pictures are shown from that sample.

On the pictures, one can observe that the deposition of the fibers is really random and there are no beads and bands among them.

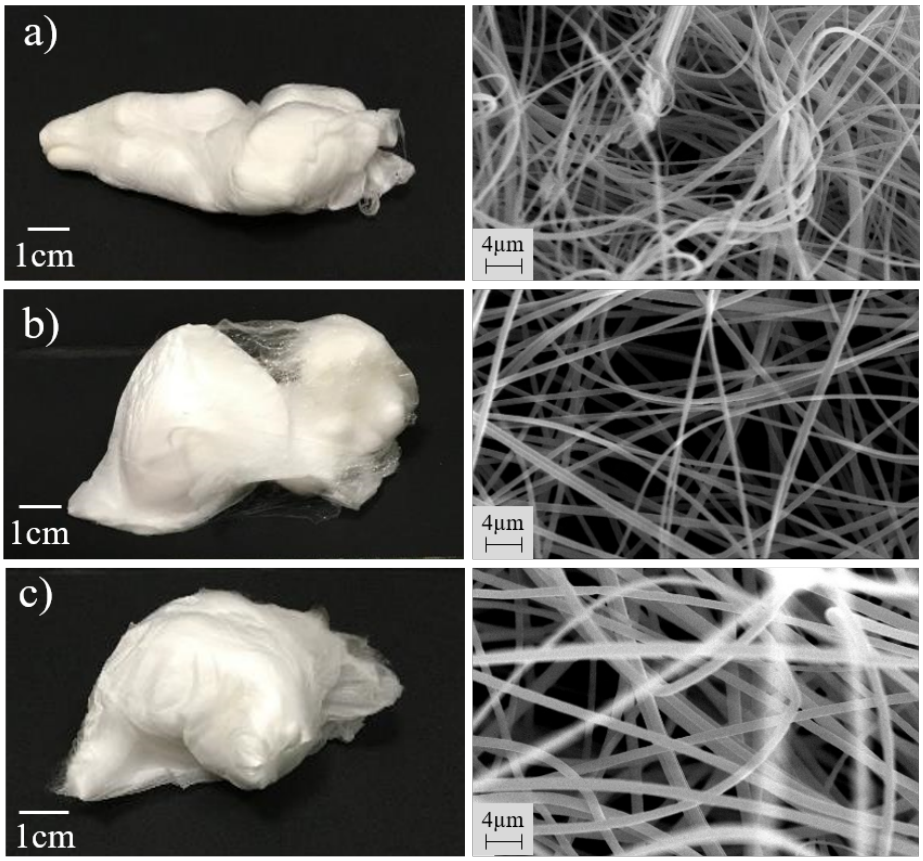

Figure 4.20 Macroscopic picture of the 3D effect of different salts used and their SEM pictures on the right a) LiCl 1 w/w% b) $MgCl_2$ 1 w/w% c) $CaCl_2$ 2 w/w%.[24]

Table 4 presents the outcome of the fiber diameter analysis. For 1 and 2 w/w% of LiCl and $CaCl_2$, there is no substantial variation, but for $MgCl_2$, all concentrations differ significantly.

Table 4 Size distribution of different fibers containing salts [24]

	Diameter [nm]		
Name of the salt	1 w/w%	2 w/w%	3 w/w%
LiCl	570±160	615±100	NA
$MgCl_2$	470±130	1230±200	625±110
$CaCl_2$	660±220	675±110	950±150

4.3.2 Vibrational spectroscopy on the PSI fibers

ATR-FTIR and FT-RAMAN spectroscopic analysis were performed on the electrospun meshes Figure 4.21. No evidence of chemical interactions can be seen in the spectra of the pure PSI fibers and those with salts. The characteristic peaks of polysuccinimide appear at 1710 cm^{-1} (asymmetric stretching vibration attributed to the νCO of $–(OC)_2N–$), 1391 cm^{-1} (C–O bending vibration, δ) and 1355 cm^{-1} (stretching vibration, νC–N of $–(OC)_2N–$), which are the bands of imide rings in PSI. The only noticeable difference observed is around the OH vibrational bands at 3300-3600 cm^{-1}.

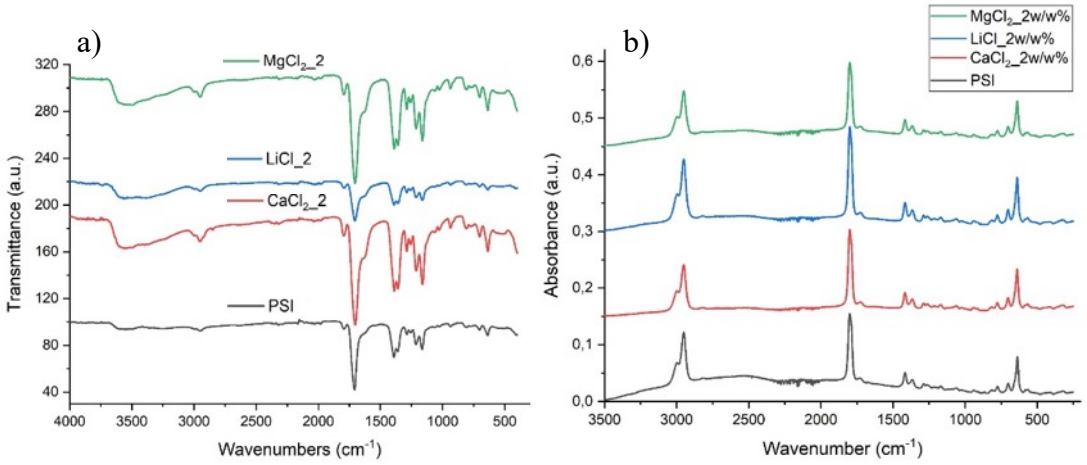

Figure 4.21 The FTIR and FT-RAMAN spectra of the different dry fibrous mesh in the presence of inorganic salts (LiCl, $MgCl_2$, $CaCl_2$) at 2 w/w% concentrations and PSI for comparison

5 Discussion

5.1. Characterization of DMF – Water mixtures in different compositions

5.1.1 Analysis of Water – water interactions as the amount of DMF increases

Figure 4.1a presents the RDF of Ow and Hw atoms as the amount of DMF increases in water, the height of two peaks in the H-bonding structure of water also increases. This is likely an indication that the presence of hydrophobic groups (CH_3 groups) in DMF enhance the strength of the H-bonds between water molecules. This behavior also can be seen in the case of the water O atoms Figure 4.1b. As DMF increases one can observe a minimum around 3.3 Å which is clear evidence of the interstitial water neighbors disappearance. These water molecules can be found in the holes of the tetrahedral H-bonding network.

On the other hand, it should be emphasized that the enhanced H- bonding structure doesn't imply stronger H-bonds since it would imply also shorter H-bonds. Secondarily, the increase of the H-bonding peaks doesn't necessarily imply the increase of the number of H bonds between H-bonds. This is due to the fact that the RDF is normalized by the density of the particles, therefore increasing the number of DMF molecules decrease the density of water which can be also follow in Figure 4.1.a inset from the coordination number of Hw around Ow. This function evidences the decline in the coordination number of Hw around Ow atoms, and the decrease in the number of H-bonds between water molecules upon dilution with DMF.

The minimum of $g_{O_wH_w}(r)$ is at around 4.2 Å, which is reflected in the gradual evolution of a second plateau of the running coordination number. This phenomenon evidences a rapid decline of the H-bonded water neighbors which are connected to the central molecule through a chain of two consecutive H-bonds, via a bridging water molecule. Therefore, the presence of the first two peaks indicates that water-water hydrogen bonds are present even at very low mole fractions. The emergence of the second minimum demonstrates the gradual breaking of longer (even 3-molecular) hydrogen-bonded water chains as the mole fraction of water decreases.

In the work of Lei et. al. similar pattern can be found. While increasing x_{DMF} the height of the two peaks also increases. They claim that below x_{DMF} =0.1 it's enhancing the structure of water, but above that DMF destroys that. Above x_{DMF} = 0.75 the tetrahydral structure of water is destroyed but dimer and trimer H-bonded water molecules can be found. [102]

Figure 4.2. shows the contributions of the first five neighbor of the water atoms. Due to increasing DMF, the closeness of two neighboring H atoms which are accepting a bonding H atom from the central molecule, causes another peak to evolve at 3 Å. This peak illustrates the growing number of water molecules that have H-acceptor neighbors rather than H-donor ones. Additionally, in line with the previously mentioned increase in the peak heights of the $g_{O_wH_w}(r)$ function, both of the first neighbor's peaks of the function also increase in height as the mole fraction of water decreases. A third peak can be observed while increasing the mole fraction of DMF around 5 and 6 Å. This peak becomes broader and shifts farther with the increase of DMF. It evidences the existence of water neighbors that are not hydrogen-bonded to the central molecule. Based on the assumption that DMF-water H-bonding distances are similar to those seen between two water molecules and a H-bonding angle of 120 degrees around the oxygen atom of the DMF molecule, the position of this peak suggests that these water neighbors are typically connected to the central water molecule through a bridging DMF molecule. However, the shift and the broadening of this peak suggests the gradual emergence of nearest water-water pairs that are not even connected through a bridging molecule. This observation implies that the decrease in the number of water molecules accepting two water-water hydrogen bonds, as opposed to just one, is not compensated by the previously mentioned enhancement of the hydrogen-bonding structure at large enough DMF mole fractions.

5.1.2 Gaussian curve fitting on the first five nearest neighbor compositions

Gaussian curve fitting was conducted on the individual peaks of the $g^{(k)}_{O_wH_w}(r)$, to quantify the results. This is shown on Figure 4.3 a-e for the increasing k values.

As the value of k and the mole fraction of DMF increase, the $g^{(k)}_{O_wH_w}(r)$ functions become more complex. The first peak of these functions, for $k \geq 3$, occurs

between 3 and 4 Å, leading to the second peak in the total RDF function. This peak, caused by non-H-bonding Ow-Hw pairs of H-bonded water neighbors, generally decreases in height as the mole fraction of DMF increases, indicating a decrease in the number of such water pairs. This peak is followed by several others located at various distances between 4 and 8 Å. This indicates the presence of water pairs connected in various ways. Also, the last peaks of these distributions occur around or above 8 Å and rapidly shift to larger distances as the DMF mole fraction increases. These peaks are caused by water neighbors that are not connected in any obvious way, and the shift in their position is simply a result of dilution. In the case of k= 3 and 4 the functions become unimodal, with only a large distance peak, at a DMF mole fraction of 0.9. For the 5^{th} neighbor this value is 0.7. This suggests that at DMF mole fractions above 0.7, water molecules have no more than 2 water neighbors that are connected to them by a H-bond or through a bridging molecule, and above a DMF mole fraction of 0.9, they have no more than 1 water neighbor.

In the work of Lei et. al. they found a similar behavior analyzing MD simulation DMF-water mixtures but on a smaller simulation system (216 molecules compared to this work which had 500). They claim that with higher number of molecules their results are more accurate. They found that above $x_{DMF} = 0.75$ the water molecules have no more than 2 H-bonds and above 0.9 it's no more than one, which is in line with my results. [102]

5.1.3 Analysis of Water-DMF and Water-Water correlation as the amount of DMF increases

In Figure 4.4 one can observe the RDF of DMF's oxygen atom and hydrogen atoms of water. The expected competition is seen from the RDF and the first five neighbors of H_w neighbors of the O_D atoms. The functions being discussed are similar to the previously mentioned in Figures 4.1.a and 4.2. As the amount of DMF increases, the height of the first two peaks in the RDF (related to molecules that form hydrogen bonds) increases, and a second minimum and a third peak appear, indicating that the structure of hydrogen bonding is becoming stronger in the presence of hydrophobic molecules and that the presence of water-bridged DMF-water pairs is diminishing. It's important to note that, like water-water hydrogen bonds, DMF-water hydrogen bonds also remain present even when the amount of water is very low.

The $g^{(k)}_{O_D H_W}(r)$ contributions resemble the behavior of the $g^{(k)}_{O_W H_W}(r)$ functions as well.

That way, in the case of the first neighbor, the height of the first peak increases as the amount of DMF increases throughout the entire range of compositions. However, when k=2, the height goes through a maximum. It is worth mentioning that the presence of the first peak of the second neighbor of the $g^{(2)}_{O_W H_W}(r)$ function even at the highest concentration of DMF considered, shows that there is a significant proportion of DMF molecules that have two water molecules as H-bonded neighbors even when the amount of water is very low.

This finding supports the previous conclusion that in systems with high concentrations of DMF, water molecules that are closely connected to DMF molecules through a bridge can also be found. For k ≥ 3, the first peak of the $g^{(k)}_{O_D H_W}(r)$ function gives rise to the second peak of the total RDF function. Additionally, several peaks occur between about 4 and 8 Å due to the various ways that DMF and water molecules are connected. Finally, at high concentrations of DMF and high values of k, the $g^{(k)}_{O_D H_W}(r)$ function becomes unimodal again, with its peak above 8 Å, and this peak shifts rapidly to larger distances as the amount of DMF increases, which indicates that the number of closely connected water neighbors of DMF decreases as the amount of water decreases. At k = 3 and k = 5, this unimodal peak occurs again at DMF concentrations of about 0.9 and 0.6, respectively. Therefore, at DMF concentrations above these concentrations, similar to water, DMF molecules also do not have more than 2 and 1 water neighbors, respectively, that are connected to it either through a hydrogen bond or through a bridge.

These findings indicate that the correlation between O_D and H_W is very similar to that of Ow and Hw, meaning that DMF oxygen atoms can effectively take the place of water oxygens in the local hydrogen bonding environment in these mixtures. This is similar to what is often observed in water-formamide mixtures, where both molecules can form hydrogen bonding networks on their own and can effectively replace each other in these networks. However, the behavior of water-DMF mixtures differs from that of water-formamide mixtures in two important ways. Firstly, due to the lack of hydrogen-donating

groups in the DMF molecule, the hydrogen bonding network breaks down as the amount of DMF increases, as evidenced by the gradual disappearance of even the short hydrogen bonding chains. Secondly, in agreement with the known structuring effect of hydrophobic groups, the presence of hydrophobic CH_3 groups leads to an enhanced hydrogen bonding structure, reflected in the observed increase in the height of the hydrogen bonding peaks in the corresponding radial distribution functions as the amount of DMF increases.

All the above analyses have shown that the hydrogen bonding network of the water molecules gradually breaks down and is replaced by water-DMF bonds as the amount of DMF increases. As can be seen, the number of water-water hydrogen bonds decreases gradually from about 900 (corresponding to about 3.6 hydrogen-bonded water neighbors of the molecules) in pure water to zero as the amount of DMF increases, while the number of water-DMF hydrogen bonds reaches a maximum at an equimolar composition, that is, when the two molecules forming such a bond are in stoichiometric proportion. In this system, a water molecule forms, on average, 2 hydrogen bonds with other waters and 1 with a DMF, while DMF molecules have, on average, 1 hydrogen-bonded water neighbor. The total number of hydrogen bonds present in the system also decreases monotonously, in accordance with the fact that DMF molecules do not have a hydrogen atom to donate to a hydrogen bond.

This discovery shows that as the amount of water increases, the hydrogen bonds formed by water-donated O-H hydrogens take over and replace the weaker hydrogen bonds formed by CH-donated H-bonds. As a result, the position of the nearest neighbor H_D atom around an O_D atom becomes progressively less well defined. This effect is also reflected in the gradual strong broadening of the $g^{(1)}_{O_D H_D}(r)$ contribution (Figure 4.7). These changes reflect the fact that as the amount of DMF decreases, the fraction of DMF molecules among the first shell neighbors decreases as well, while the arrangement of the remaining DMF neighbors around each other remains essentially unchanged.

5.1.4 Analysis of the local surroundings with Voronoi Polyhedra method

Figure 4.9 illustrates how the volume of the VP changes when analyzing all molecules, only water molecules, and only DMF molecules($P(V)$, $P_w(V)$, and $P_D(V)$, respectively). When considering all molecules, there is a gradual shift in the distribution between water and DMF as the composition of the system changes. The difference in

peak positions between the two systems is due to the fact that the density of water molecules is much higher than that of DMF molecules.

When either of the two components is added to the pure liquid of the other component, the distribution shows an extension on one side of the distribution (on the side of larger V values when adding DMF to water, and on the side of smaller V when adding water to DMF). As more of the minor component is added, this extension caused by the VP of the minor component, turns into a shoulder and eventually becomes a distinct second peak. These two peaks become roughly the same height at $x_{DMF} = 0.4$, near the point of equal amounts of the two components.

At the same time, the main peak of the distribution moves to higher V values in the case of mixtures that are rich in water, and to lower values in the case of mixtures that are rich in DMF. This demonstrates that the fraction of minor component molecules in the local environment of the major component molecules is increasing. The smooth transition of the distribution indicates that, similar to the case of water-DMSO mixtures, but unlike that of acetone-methanol mixtures, the two components mix with each other on a molecular level. [96,103]

This observation can be further refined by studying the $P_w(V)$ and $P_D(V)$ distributions. These distributions show a gradual shift to higher values and a widening with decreasing mole fraction of the component being considered, resulting from dilution. It is worth to highlight that, these distributions do not display a distinct, long tail with a decreasing mole fraction of either of the two components (as seen in the insets of Figure 4.9, which confirms that the system lacks microheterogeneities.

When the amount of a specific component is high, the peak of the distribution changes gradually, which means that a significant portion of the major component's molecules still have a similar environment to that of the pure liquid. This is particularly noticeable in the case of DMF, where the $P_D(V)$ distribution does not change much even when the proportion of DMF is as low as 0.4-0.5. This implies that in systems where DMF is the dominant component, there are still areas where the molecules of DMF group together in a way that their surroundings are similar to those in pure DMF.

A similar pattern is observed in the void radius distributions, shown in Figure 4.10 as obtained with all molecules as well as when considering only water or only DMF molecules in the analysis (P(R), Pw(R), and $P_D(R)$, respectively). These distributions

describe the local environment of the intermolecular voids rather than that of the molecules themselves. It is noteworthy that up to an x_{DMF} value of about 0.2, the peak of the P(R) distribution occurs roughly at the same position, indicating that in these water-rich systems, the majority of the voids are in a water-like local environment; those located in mixed environments (surrounded by both types of molecules) only contribute to the gradually extending tail. Additionally, the distributions obtained at the DMF-rich end of the composition range ($x_{DMF} \geq 0.8$) are also similar to each other, indicating that here the majority of the voids are surrounded by DMF molecules.

This effect is even more apparent in the $P_w(R)$, and $P_D(R)$ distributions. The peak of the $P_w(R)$, and $P_D(R)$ distribution in pure water persists up to $x_{DMF} = 0.3$ and transforms into a shoulder that is visible up to $x_{DMF} = 0.5$, indicating the existence of voids that are surrounded solely by water molecules up to the equimolar composition. Similarly, the $P_D(R)$ distribution shows very little changes above $x_{DMF} = 0.5$, indicating that in DMF-rich mixtures the majority of the voids are also located in pure DMF-like environment.

The results from the analysis of the asphericity parameter distribution, as seen in Figure 4.11, confirms the previous findings from the radial distribution function analysis ($P(\eta)$, $P_w(\eta)$, and $P_D(\eta)$, respectively). When comparing the two pure systems, the peak of the $P(\eta)$ distribution is found at higher values η for water molecules (1.65) as compared to DMF molecules (1.55). This is because water molecules are usually surrounded by four neighboring molecules that are arranged in a tetrahedral shape, while DMF molecules have around 12 neighboring molecules, which creates a more spherical environment for the latter.

When DMF is added to water, the asphericity parameter distribution extends to even larger η values, indicating that some of the H-bonded water neighbors are replaced by DMF, resulting in a less spherical environment for the central water molecule. This effect is more pronounced when looking at the $P_w(\eta)$ distribution, as the disregarded DMF neighbors are treated as empty space, making the apparent environment of the water molecules even more aspheric. The gradual increase in the tail of the $P_w(\eta)$ distribution at large η values is a clear indication of the growing fraction of water molecules that have both H-bonded water and DMF neighbors.

When all of the H-bonded neighbors of a water molecule are replaced by DMF, and the nearest water neighbors are distant and non-H-bonded, the apparent local

environment is more spherical than when some H-bonded water neighbors are present. As a result, the peak of the $P_w(\eta)$, distribution shifts to lower values as the DMF mole fraction increases beyond 0.3, despite having initially shifted to larger values compared to neat water. However, the fact that the distribution still has a long tail at large η values even at x_{DMF} = 0.9 suggests that H-bonded water pairs are still present at the high DMF mole fraction end of the composition range.

5.2. Characterizing the salt-DMF correlation

Electrospinning technology has undergone significant advancements, including the optimization of apparatus design and process parameters. The use of salts is a common strategy to improve the electrospinnability of polymers, and the type and concentration of salt can alter the thickness and surface roughness of the resulting fibers. Additionally, salts can facilitate the dissolution of certain polymers. In some cases, the use of salts has resulted in the formation of small three-dimensional structures rather than the expected two-dimensional layer.

5.2.1 Solubility range of salt-DMF

To investigate the impact of anions and cations on 3D formation, a range of halide and chloride salts were selected based on their solubility in DMF. Since the solubility values in the literature varied, I created a general solubility curve to determine the solubility limit in laboratory conditions (Table 2). In the case of LiBr, saturation occurred at 8w/w% and in the case of LiCl, salt crystals appeared due to the influence of environmental parameters during storage (at 9 and 10 w/w%). As expected, the yellow color deepened as the concentration of iodide salts increased.

5.2.2 Measuring the conductivity of salt-DMF mixtures

The conductivity of a polymer solution plays a role in the electrospinning process, influencing the stability of the electric field and the resulting fiber properties. High conductivity solutions may lead to unstable jet formation and over-stretched fibers, while low conductivity solutions may result in poor fiber formation.[104] The conductivity of the solution can also affect the charge density and diameter of the fibers, as well as the rate of solvent evaporation during the electrospinning process. Interestingly, as can be seen in Figure 4.13 the salts with the lower conductivity resulted 3D formations.

Considering the compatibility with living systems, we chose to conduct the experiments using LiCl, $CaCl_2$, and $MgCl_2$ due to the presence of chloride as the co-ion.

5.2.3 Analysing salt-DMF mixtures with vibrational spectroscopy

Vibrational spectroscopy is an effective method for the investigation of ion-ion and ion-solvent interactions through the analysis of modifications in the characteristics of specific vibrational modes, including shifts in frequency, intensity, and peak width. This method enables the characterization of the nature and strength of intermolecular interactions in a variety of systems. [49,105,106]

The intense C=O vibration is inherently asymmetric and skewed negatively, as indicated by the presence of spectral contribution at lower wavenumbers (~1640 cm^{-1}). As depicted in Figure 4.15, this vibrational mode undergoes a shift towards lower wavenumbers upon coordination with Li^+, Ca^{2+} or Mg^{2+}. However, it is challenging to accurately determine the extent of this wavenumber shift due to the overlap of this vibrational mode with both the overtone of the C-N vibrational mode (Fermi coupling) at 865 cm^{-1} and the C-H deformation. [107,108]

There are several mechanisms that make it difficult to use the C=O vibrational mode as a means of analyzing ion-DMF interactions with certainty. These mechanisms include dipole-dipole interactions, the failure of the Fermi-coupling condition, and specific interactions involving the cation and the O atom. As a result, it is necessary to use an alternative vibrational mode for the analysis of ion-DMF interactions. One such mode is the $NC^{H}=O$ bending peak, which has been found to be a suitable indicator of these interactions.

Phadke et. al also describes this peak when analyzing the behavior of LiCl, $ZnCl_2$, $AlCl_3$ salts in DMF. They claim that the magnitude of the observable shifts and changes correlates to the ionic radii of the various ions. Next to the DMF $NC^{H}=O$ bending peak another peak appears gradually with the increase of the salts's concentration. The appearance of this new peak is due to complex forming between solvent-salt and salt-salt molecules. [49]

5.2.4 Gaussian curve fitting of the observed peaks

In order to quantify the changes in the range of wavenumbers in this domain, I performed a fit of the spectra in this region, assuming the presence of two spectral

contributions. The position and intensity of these contributions are shown in Figure 4.16a for each salt-DMF mixture. This figure illustrates that the position of the main peak is not affected by either the nature of the salt or its concentration. This is consistent with the interpretation that this peak is primarily associated with DMF molecules that are surrounded mainly by other DMF molecules, with the salt being at a farther distance from a reference DMF molecule.

The position of the new peak, located at higher wavenumbers, depends on the nature of the salt. The $MgCl_2$ salt-DMF mixture exhibits a large upshift, suggesting that the DMF molecules are more tightly bound to $MgCl_2$ than they are to LiCl or $CaCl_2$. This indicates that the nature of the salt can influence the strength of the interactions between the DMF molecules and the ions.

Forero et al. observed a similar trend in the case of the mixture of DMF and salts containing the same cations in combination with bis(trifluoromethanesulfonyl)imide (TFSI, anion). However, they found a much larger shift compared to data presented here. This suggests that the new peak at higher wavenumbers is associated with both the cation and the anion interacting with DMF. This indicates that the nature of both the cation and the anion can influence the strength of the interactions between the ions and the DMF molecules.[109]

One parameter that can be used to quantify the strength of the ion-DMF interactions is the ratio Z/r_c proposed by Waghorne et al., where Z is the charge of the cation and r_c is its radius. For Li^+, Ca^{2+}, and Mg^{2+} cations, the values of this ratio are 1.67, 2.02, and 3.08, respectively. The data suggests that the ion-DMF interactions are the strongest for the $MgCl_2$ salt, as indicated by the largest shift in wavenumber observed in Figure 4.16a. This finding supports the hypothesis that the strength of these interactions can be affected by the charge and size of the ions. These results highlight the importance of considering both the charge and size of the ions when analyzing the strength of ion-DMF interactions. [110]

Figure 4.16b displays the concentration-dependent intensity ratio between the new peak (IH) and the main peak (IM). This figure illustrates that the population of DMF molecules close to the cation increases relative to the population of DMF molecules in the bulk or surrounded by other DMF molecules that are too far from the cation to be influenced by it. The data also suggests that there are more DMF molecules in complex

with Li^+ cations compared to those in complex with Ca^{2+} and Mg^{2+} cations. These findings suggest that the proximity of the DMF molecules to the cation and the nature of the cation can both play a role in the formation of complexes between the ions and the DMF molecules.

5.2.5 Intermolecular interactions between salt-DMF mixture

To investigate the key characteristics of intermolecular interactions in salt-molecular solvent mixtures, DFT calculations were carried out on a set of representative configurations. These configurations were designed to simulate various environments while minimizing computational cost. The first configuration consists of 4 DMF molecules, while the remaining three configurations each feature a pair of LiCl, $MgCl_2$, or $CaCl_2$ with 4 DMF molecules. These calculations allow for the examination of the interactions between the ions and the DMF molecules under different conditions.

The representative configurations of salt-molecular solvent mixtures were designed to mimic the conditions of pure DMF and very high concentration (saturated) DMF-salt mixtures. The optimized geometries are depicted in Figure 4.17. Unlike many previous calculations, the anion was included in these configurations. [111–113]These calculations allow for the investigation of the intermolecular interactions under a range of conditions, including pure DMF and highly concentrated DMF-salt mixtures.

Due to the limited number of ions and DMF molecules included in the calculations, it is important to distinguish between the geometrical and wavenumber values of atoms that are located at the border of the configurations (and are not interacting with their environment) and those located in the core of the configurations (and are experiencing interactions with their neighbors). This distinction is necessary to accurately interpret the results of the calculations.

Table 3 lists the maximum and minimum values of intramolecular distances and the frequencies of the C=O, C-H, and NC^{H}=O modes. The table also includes the two lowest values of the intermolecular distances, which describe the ion-DMF interactions. These values provide insight into the behavior of the ions and DMF molecules under different conditions and can be used to understand the nature of the interactions between these species. In the work of Rao et. al. one can find the distances of cations and the oxygen measured experimentally and it's very close to the calculated distances (LiCl

Calculated: 1.947, 1.951 Experimental: 1.949, 1.952; $CaCl_2$ Calculated: 2.269, 2.318 Experimental: 2.341; $MgCl_2$ Calculated: 2.004, 2.068 Experimental: 2.006, 2.064). [114]

To understand the preferential interactions between the cations or anions and the DMF molecules, we examined the resonance structure of DMF. This structure reveals that the negative and positive charges are located at the oxygen and nitrogen atoms, respectively, and is accompanied by a decrease in the C=O distance and an increase in the C-N distance. The changes in the intramolecular distances can be used as indicators of the strength of the ion-DMF interactions. By analyzing the resonance structure of DMF and the resulting changes in intramolecular distances, it is possible to gain insight into the nature of the interactions between the ions and DMF molecules.

The behavior of the intramolecular distances and their corresponding frequencies allows for ranking of the salt-DMF interactions in the same order as previously mentioned. The distances between the ions and the O, N, and H atoms of the $NC^{H}=O$ amide moiety are the result of the balance between their electrostatic repulsive and attractive interactions. These distances are depicted in Figure 4.17 and are provided in more detail in Table 3. The analysis of these values suggests the following general trend: the cation is closer to the O atom than the anion, while the anion is closer to the N atom than the cation. This suggests that the nature of the ion can influence the distance between the ion and the atoms of the DMF molecules.

In order to explain the trend in the C=O vibrational mode in the salt-DMF mixtures, I considered both the intermolecular distance between the cation and the O atom and the angle ∠cation …O=C the values of which are shown in Table 3. These factors may help to explain the behavior of the C=O vibrational mode and how it is impacted by the presence of ions.

The shift of the C=O vibrational mode appears to be primarily influenced by the orientation of the cation relative to the C=O bond. When the angle between these species is large (the configuration tends towards being linear), the extent of the shift increases. This suggests that the orientation of the cation plays a key role in determining the behavior of the C=O vibrational mode.

The behavior of the C=O vibrational mode is also found to be correlated with the ratio Z/r proposed by Waghorne et al., where r is the distance between the cation and the O atom of DMF as determined by the DFT calculations (see Table 3). The values of this

ratio are 0.51, 0.68, and 0.99 for Li^+, Ca^{2+}, and Mg^{2+}, respectively. This suggests that the strength of the ion-DMF interactions, as quantified by the ratio Z/r, may also influence the behavior of the C=O vibrational mode. [110]

This finding is consistent with the observed significant downshift of the C=O vibrational mode in the $MgCl_2$ mixture. This suggests that the strength of the ion-DMF interactions, as well as the orientation of the cation, may both contribute to the shift of the C=O vibrational mode.

The degree to which the wavenumber of the C-H bending mode (~1400 cm^{-1}) shifts to lower values appears to be correlated with the short distance between the anion and the H atom. When this distance is shorter, as is the case for $MgCl_2$, the calculated C-H bending is lower. This suggests that the strength of the ion-DMF interactions, specifically the distance between the anion and the H atom, may influence the shift of the C-H bending mode.

It is difficult to rationalize the higher wavenumber shift of the $NC^H{=}O$ bending mode due to its strong overlap with another vibrational mode. The behavior of this mode is likely influenced by the interaction of both the cation and the anion with the O and H atoms of the $NC^H{=}O$ group. In the case of $MgCl_2$, the calculated $NC^H{=}O$ vibrational is the highest among the studied salts, which may be due to the short distance of the cation from the O and H atoms compared to the distance involving the anion. This suggests that the strength of the ion-DMF interactions, specifically the distance between the ions and the O and H atoms, may affect the shift of the $NC^H{=}O$ bending mode.

5.3. Creating 3D electrospun fiber meshes

After conducting extensive experiments to evaluate the properties of salt-solvent solutions, fibrous structure were attempted to create. As previously noted, only a limited number of publications have reported successfully creating 3D fluffy electrospun meshes. The macroscopic structure of the fibrous material was generally similar across all the cases studied, as illustrated in Figure 4.20. SEM analysis revealed that the fibers had smooth surfaces and consistent diameters. However, while using $MgCl_2$, I encountered an issue known as gelation during the electrospinning process. This occurrence is a well-known in polymer science and medical science, as both Mg^{2+} and Ca^{2+} ions can create physical crosslinks between polymer chains, resulting in a gel-like structure. [115] In the

current system, the Mg^{2+} ions resulted in an inhomogeneous structure during the fiber formation process, while the fluffy structure formation was reproducible, the fiber formation altered over time, and the fiber diameter varied. It is noteworthy that LiCl also led to gelation at concentrations above 3 w/w%, however, below that concentration, the fibrous structure clearly formed without any increase in viscosity over time, as shown in Figure 4.20. For $MgCl_2$, the 3D structure only appeared when the concentration reached 1 w/w%, whereas above 3 w/w% salt content, gelation occurred almost immediately after mixing the solution with the polymer, preventing electrospinning.

According to Kim D. Collins Mg^{2+} has the highest affinity to water with a *B*-coefficient = 0.38 and can bind to 5 water molecules. Ca^{2+} is next in line with a *B*=0.285, and can bind to 2 water molecules. In contrast, Li^{+} has only *B* = 0.150 and can bind to 0.6 water molecule. In contrast to this, LiCl has the highest hygroscopicity of all three. [116–118] Since humidity is not controlled during the electrospinning process, it can lead to unfavorable outcomes as discussed. To understand the whole process on the molecular level, molecular modeling can definitely help. That is why it was the first step to analyze the water-solvent, and solvent-salt behavior since during electrospinning water vapor, the evaporating solvent, the salt and the polymer is present at the same time.

The fibrous structure created using $MgCl_2$ was inhomogeneous at all concentrations, but it was more compact than the structure formed using LiCl. In terms of reproducibility, $CaCl_2$ in the 1-3 w/w% concentration range provided the best results. At all concentrations, $CaCl_2$ resulted in a fluffy and sponge-like structure. At the highest concentration (3 w/w%), the 3D expansion was the highest among all the compounds tested. After turning off the electric field, the meshes temporarily collapsed slightly (less than 10%), but they retained their shape and structure for over a year.

When comparing the molarity of different salts in Table 2, it was found that the $CaCl_2$ and $MgCl_2$ systems were able to create a 3D fluffy structure at very low concentrations (around 0.1 mol/L in DMF) in comparison to LiCl, which needed a concentration of 0.23 mol/L in DMF to produce a similar structure. Using the ratio Z/r, proposed by Waghorne et al. as a measure of the interaction strength between the DMF and cation (where Z is the cation charge and r is its radius), it is clear that the molarity of the salts can be better understood based on the above mentioned computational simulations. [110] The values for Li^{+}, Ca^{2+} and Mg^{2+} are 1.67, 2.02 and 3.08 respectively

as it was shown earlier. This highlights that Mg^{2+} and Ca^{2+} cations, which have slightly larger ionic radii but double the charge of Li^{+}, can produce a 3D effect at lower concentrations. The interaction between the cation and the DMF molecule is highly affected by the charge, which means that less moles are needed to achieve the same fluffy result, which is in a good agreement with the simulations.

5.3.1 Analysis of the average fiber diameter with Scanning Electron Microscopy

Data on fiber diameter analysis is presented in Table 3, where it's seen that for both LiCl and $CaCl_2$, there is no significant difference between concentrations of 1 and 2 w/w%. But for $MgCl_2$, all 3 concentrations were significantly different, with 2 w/w% being outside of the range. Similarly, 3 w/w% $CaCl_2$ caused a significant increase in diameter, but also appears to be out of range. Based on the available data and statistical analysis, there appears to be little to no effect of salt concentration on the average diameter.

Addition of different salts to the solution leads to higher conductivity and leads to thinner, uniform fibers most of the time. But there are some opposite experiences when adding salts to the system. [50,52,119,120]

In the work of Mit-uppatham et. al. they studied the effect of different solution conditions on electrospinning of Polyamide-6 fibers. Increasing LiCl the conductivity, the viscosity, and the fiber diameter increased gradually. While adding $MgCl_2$ the conductivity increased as well the fiber diameter but the viscosity varied. Change in viscosity also can affect fiber diameter, therefore it confirms the variation in the resulted fiber diameter with $MgCl_2$. They claim that the increase of viscosity also suggests an increase in electrostatic and Coulombic forces too. It would also suggest that the fiber diameters should decrease. The increase of the viscoelastic force and the the mass flow could be the explanation of this behavior. [120]

5.3.2 Analysis of the final fiber meshes with vibrational spectroscopy

The results of the analysis revealed that none of the salts were present in the dry form and there were no traces of DMF detected which is important to avoid for biomedical applications, especially for tissue engineering. Therefore, according to the FTIR and FT-RAMAN spectra (Figure 4.21), there are no observable chemical interactions between the

salt and the polymer beyond the detection limit of the instrument. The main difference in fiber formation appeared to be based on the properties of the salt and the interactions between the salt and solvent. Therefore, after creating the fibers, the differences in formation were no longer observable in the spectrum as the solvent had evaporated. The only indication of the presence of salt being retained is the fiber diameter.

6 Conclusions

New scientific accomplishments are summarized in the following points:

T1. The local structure of DMF-water mixtures of various concentrations were investigated with radial distribution function, nearest neighbor and Voronoi polyhedra methods from Molecular dynamics simulation. The results show that while there's a tendency of self-association, generally the two component mix well on the molecular scale. Water-water clusters of no more than 3 and 2 molecules disappearing around DMF mole fraction values of 0.7 and 0.9 respectively. Additionally, DMF molecules form weak, C-H….O type hydrogen bonds with each other in their neat liquid but upon addition of water, these weak H-bonds gradually disappear, because the water molecules can form considerably stronger, O-H….O type hydrogen bonds with the DMF oxygens. [JAGy1]

T2. DMF-salt interactions were characterized with DFT calculations. The interatomic distances and frequencies of the C=O, C-H, and NC^{H}=O modes were specified. The analysis of the distances suggest that the cation is closer to the O atom than the anion, while the anion is closer to the N atom of the DMF than the cation. Generally, the ion-solvent interaction is responsible for the observed shifts but in the case of C=O vibrational mode it's also orientation of the cation. In the case of C-H bending mode it's also the distance of the anion from H atom, and lastly with the NC^{H}=O bending mode it's also the distance between the ions and the O and H atoms. The results show that the intermolecular interaction strength with DMF of the salts increase in the following order LiCl < $CaCl_2$< $MgCl_2$. [JAGy2]

T3. DMF-salt interactions were characterized with vibrational spectroscopy. The results show that the intense C=O vibrational is asymmetric and skewed negatively (~1640 cm^{-1}), due to coordination with Li^+, Ca^{2+} or Mg^{2+}. Another characteristic peak of DMF NC^{H}=O bending peak (660 cm^{-1}) shows a new peak formation very close at 675 cm^{-1}, which can be explained by the complex forming between solvent-salt and salt-salt molecules. The $MgCl_2$ salt-DMF mixture exhibits a large upshift in binding strength between the DMF molecules and the ions, indicating that the nature of the salt can influence the strength of these interactions. The data suggests that there are more DMF molecules forming complexes with Li^+ cations than with Ca^{2+} and Mg^{2+} cations, indicating that both

the proximity of the DMF molecules to the cation and the nature of the cation can play a role in complex formation. [JAGy2]

T4. 3D PSI meshes were electrospun reproducibly, and characterized with SEM and Vibrational spectroscopy in the presence of $CaCl_2$, $MgCl_2$ and LiCl. The results from FTIR and FT-RAMAN show that there is no chemical change in the end of the electrospinning process, and there's no sign of DMF therefore the fiber meshes are solvent free. The SEM results shows an increase in fiber diameter in the case of $CaCl_2$ (1w/w%: 660±220nm; 2w/w%: 675±110nm; 3w/w%: 950±150nm) and LiCl (1w/w%: 570±160; 2w/w%: 615±100), in the case of $MgCl_2$ (1w/w%: 470±130; 2w/w%: 1230±200; 3w/w%: 625±110) it varies greatly, and from the statistical analysis it seems that there's no correlation with the salt concentration and the fiber diameter. $CaCl_2$ is found to be the best candidate to use since it's biocompatible and gelation was not observed during preparation resulting better macroscopic 3D structures. [JAGy2]

7 Summary

3D scaffold produced by electrospinning mimic the native extracellular matrix, has better processability than conventional electrospinning. For tissue engineering applications would be ideal to use these scaffolds although the causes of this phenomena are still uncovered. Therefore, my aim was to create and characterize 3D electrospun fibers with electrospinning technique and investigate the behavior of the solvent salt and solvent-water interactions with different computational simulation methods.

Firstly, I analyzed DMF-water mixtures of various compositions from the molecular dynamics simulation data with radial distribution, nearest neighbor and Voronoi polyhedra methods. The results clearly show that DMF mix very well with water on molecular scale, while there's some tendency for self-association even in their dilute systems. The water-water H-bonds are remains while increasing DMF mole fraction values parallel the water clusters are disappearing. This is explained by the increasing CH_3 groups enhance H-bonding structure, and also by the DMF's O atoms can easily replace water oxygens.

Then, I characterized the DMF-salt interactions with DFT calculations and Vibrational spectroscopy. Unlike before, the anion was also included to the calculation. While the concentration of the salt in DMF was quite saturated, the results are align with experimental data. Both the calculated and the experimental data suggest that $MgCl_2$ tends to have the strongest interaction with DMF (and also water) molecules, while all of them forms complexes with the solvent molecule. Only the salts where complex forming can be found produced 3D structure during electrospinning method, therefore the quality of the salt and its interaction with the solvent molecule is a key to a successful outcome, not just charge accumulation as thought before.

Lastly, I reproducibly created solvent free 3D PSI meshes and characterized with SEM and Vibrational spectroscopy. While one can observe a difference in fiber diameter, from the statistics there's no correlation with the salt concentration. While gelation occurs at some cases, $CaCl_2$ can be a good candidate in the future to better optimize the electrospinning parameters and used for biomedical applications.

These findings can lead to the final understanding how the 3D structure can be achieved with different polymers however there' still a lot of work ahead.

8 Résumé

Les matrices 3D produites par électrospinning imitent la matrice extracellulaire native et sont plus faciles à traiter que les matrices conventionnelles. Pour les applications d'ingénierie tissulaire, il serait idéal d'utiliser ces matrices, bien que les causes de ce phénomène soient encore inconnues. Par conséquent, mon objectif était de créer et de caractériser des fibres 3D par électrospinning et d'étudier le comportement des interactions solvant-sel et solvant-eau avec différentes méthodes de simulation numérique.

Tout d'abord, j'ai analysé les mélanges DMF-eau de différentes compositions à partir des données de simulation de dynamique moléculaire avec les méthodes de distribution radiale, du plus proche voisin et du polyèdre de Voronoï. Les résultats indiquent clairement que le DMF se mélange très bien avec l'eau à l'échelle moléculaire, alors qu'il y a une certaine tendance à l'auto-association même dans leurs systèmes dilués. Les liaisons H entre l'eau et l'eau restent alors que les valeurs de fraction molaire de DMF augmentent parallèlement à la disparition des clusters d'eau. Ceci s'explique par l'augmentation des groupes CH3 qui renforcent la structure des liaisons H, et aussi par le fait que les atomes O du DMF peuvent facilement remplacer les oxygènes de l'eau.

Ensuite, j'ai caractérisé les interactions DMF-sel avec des calculs DFT et la spectroscopie de vibration. Contrairement à ce qui s'était passé avant, l'anion a également été inclus dans le calcul. Bien que la concentration du sel dans le DMF soit assez saturée, les résultats sont alignés avec les données expérimentales. Les données calculées et expérimentales suggèrent que le $MgCl_2$ tend à avoir l'interaction la plus forte avec les molécules de DMF (et aussi d'eau), alors que tous les sels forment des complexes avec la molécule de solvant. Seuls les sels où la formation de complexes peut être trouvée ont produit une structure 3D pendant la méthode d'électrospinning, donc la qualité du sel et son interaction avec la molécule de solvant est une clé pour un résultat réussi, et pas seulement l'accumulation de charge comme on le pensait auparavant.

Enfin, j'ai créé de manière reproductible des structures 3D PSI sans solvant et les ai caractérisées par MEB et spectroscopie vibratoire. Bien que l'on puisse observer une différence dans le diamètre des fibres, d'après les statistiques, il n'y a aucune corrélation avec la concentration en sel. Bien que la gélification se produise dans certains cas, le $CaCl_2$ peut être un bon candidat à l'avenir pour mieux optimiser les paramètres d'électrospinning et être utilisé pour des applications biomédicales.

Ces résultats peuvent conduire à la compréhension finale de la façon dont la structure 3D peut être réalisée avec différents polymères, mais il reste encore beaucoup de travail à faire.

9 References

[1] N. Huebsch, D.J. Mooney, Inspiration and application in the evolution of biomaterials, Nature. 462 (2009) 426–432. https://doi.org/10.1038/nature08601.

[2] H. Kaul, Y. Ventikos, On the genealogy of tissue engineering and regenerative medicine, Tissue Eng. - Part B Rev. 21 (2015) 203–217. https://doi.org/10.1089/ten.teb.2014.0285.

[3] W.R. Wagner, S.E. Sakiyama-Elbert, G. Zhang, M.J. Yaszemski, Biomaterials science : an introduction to materials in medicine, n.d.

[4] B. Bhaskar, P.S. Rao, N. Kasoju, V. Nagarjuna, R.R. Baadhe, Biomaterials in Tissue Engineering and Regenerative Medicine, Springer Singapore, 2021. https://doi.org/10.1007/978-981-16-0002-9.

[5] B. Basu, Biomaterials Science and Implants, Springer Singapore, 2020. https://doi.org/10.1007/978-981-15-6918-0.

[6] H. Qu, H. Fu, Z. Han, Y. Sun, Biomaterials for bone tissue engineering scaffolds: A review, RSC Adv. 9 (2019) 26252–26262. https://doi.org/10.1039/c9ra05214c.

[7] R. Lanza, Principles of Tissue Engineering, 2014.

[8] T.J. Keane, S.F. Badylak, Biomaterials for tissue engineering applications, Semin. Pediatr. Surg. 23 (2014) 112–118. https://doi.org/10.1053/j.sempedsurg.2014.06.010.

[9] D.F. Williams, On the mechanisms of biocompatibility, Biomaterials. 29 (2008) 2941–2953. https://doi.org/10.1016/j.biomaterials.2008.04.023.

[10] D. Williams, Revisiting the definition of biocompatibility, Med. Device Technol. 14 (2003) 10—13. http://europepmc.org/abstract/MED/14603712.

[11] M. Zrinyi, T. Gyenes, D. Juriga, J. Kim, Acta Biomaterialia Volume change of double cross-linked poly (aspartic acid) hydrogels induced by cleavage of one of the crosslinks Thermal treatment, Acta Biomater. 9 (2013) 5122–5131. https://doi.org/10.1016/j.actbio.2012.08.046.

[12] K. Molnar, C. Voniatis, D. Feher, G. Szabo, R. Varga, L. Reiniger, D. Juriga, Z. Kiss, E. Krisch, G. Weber, A. Ferencz, G. Varga, M. Zrinyi, K.S. Nagy, A. Jedlovszky-Hajdu, Poly(amino acid) based fibrous membranes with tuneable in vivo biodegradation, PLoS One. 16 (2021) 1–21. https://doi.org/10.1371/journal.pone.0254843.

[13] E. Sipos, A. Juhasz, M. Zrinyi, Characteristic load-elongation behavior of weak electrospun fiber texture, J. Mol. Liq. 329 (2021) 115459. https://doi.org/10.1016/j.molliq.2021.115459.

[14] L. Mészáros, B. Tatár, K. Toth, A. Földes, K. S. Nagy, A. Jedlovszky-Hajdu, T. Tóth, K. Molnár, Novel, injection molded all-polyethylene composites for potential biomedical implant applications, J. Mater. Res. Technol. 17 (2022) 743–755. https://doi.org/10.1016/j.jmrt.2022.01.051.

[15] I.J. Hall Barrientos, E. Paladino, P. Szabó, S. Brozio, P.J. Hall, C.I. Oseghale, M.K. Passarelli, S.J. Moug, R.A. Black, C.G. Wilson, R. Zelkó, D.A. Lamprou, Electrospun collagen-based nanofibres: A sustainable material for improved antibiotic utilisation in tissue engineering applications, Int. J. Pharm. 531 (2017) 67–79. https://doi.org/10.1016/j.ijpharm.2017.08.071.

[16] J.L. Hernandez, K.A. Woodrow, Medical Applications of Porous Biomaterials: Features of Porosity and Tissue-Specific Implications for Biocompatibility, Adv. Healthc. Mater. 11 (2022) 1–25. https://doi.org/10.1002/adhm.202102087.

[17] J. Rnjak-Kovacina, A.S.S. Weiss, Increasing the pore size of electrospun scaffolds, Tissue Eng. B, Rev. 17 (2011) 365–372. https://doi.org/10.1089/ten.teb.2011.0235.

[18] R. Pázmány, K.S. Nagy, Á. Zsembery, A. Jedlovszky–Hajdu, Ultrasound induced, easy-to-store porous poly(amino acid) based electrospun scaffolds, J. Mol. Liq. 359 (2022). https://doi.org/10.1016/j.molliq.2022.119243.

[19] A. Frenot, I.S. Chronakis, Polymer nanofibers assembled by electrospinning, Curr. Opin. Colloid Interface Sci. 8 (2003) 64–75. https://doi.org/10.1016/S1359-0294.

[20] P. Gosh, FUNDAMENTALS OF POLYMER SCIENCE, Polymer Study Centre "Arghya" 3, kabi Mohitlal Road P.P. Haltu, Kolkata- 700078 (21.09.2006), 2006.

[21] Z.-M.M. Huang, Y.-Z.Z. Zhang, M. Kotaki, S. Ramakrishna, A review on polymer nanofibers by electrospinning and their applications in nanocomposites, Compos. Sci. Technol. 63 (2003) 2223–2253. https://doi.org/10.1016/S0266-3538(03)00178-7.

[22] K. Molnar, A. Jedlovszky-Hajdu, M. Zrinyi, S. Jiang, S. Agarwal, Poly(amino acid)-Based Gel Fibers with pH Responsivity by Coaxial Reactive Electrospinning, Macromol. Rapid Commun. 38 (2017) 1–5.

https://doi.org/10.1002/marc.201700147.

[23] K. Molnar, D. Juriga, P.M. Nagy, K. Sinko, A. Jedlovszky-Hajdu, M. Zrinyi, Electrospun poly(aspartic acid) gel scaffolds for artificial extracellular matrix, Polym. Int. 63 (2014) 1608–1615. https://doi.org/10.1002/pi.4720.

[24] A.G. Juhasz, K. Molnar, A. Idrissi, A. Jedlovszky-Hajdu, Salt induced fluffy structured electrospun fibrous matrix, J. Mol. Liq. 312 (2020) 113478. https://doi.org/10.1016/j.molliq.2020.113478.

[25] G.C. Rutledge, S. V. Fridrikh, Formation of fibers by electrospinning, Adv. Drug Deliv. Rev. 59 (2007) 1384–1391. https://doi.org/10.1016/j.addr.2007.04.020.

[26] Z. Németh, Elektrosztatikus szálképzéssel előállított poliaminosav alapú háló k tulajdonságainak vizsgálata, TDK Dolg. (2016).

[27] D. Juriga, K. Nagy, A. Jedlovszky-Hajdú, K. Perczel-Kovách, Y.M. Chen, G. Varga, M. Zrínyi, Biodegradation and Osteosarcoma Cell Cultivation on Poly(aspartic acid) Based Hydrogels, ACS Appl. Mater. Interfaces. 8 (2016) 23463–23476. https://doi.org/10.1021/acsami.6b06489.

[28] T. Gyenes, V. Torma, B. Gyarmati, M. Zrínyi, Synthesis and swelling properties of novel pH-sensitive poly(aspartic acid) gels, Acta Biomater. 4 (2008) 733–744. https://doi.org/10.1016/j.actbio.2007.12.004.

[29] E. Kny, K. Ghosal, S. Thomas, Electrospinning: From Basic Research to Commercialization, 2018. https://doi.org/10.1039/9781788010580-FP007.

[30] N. Tucker, K. Hofman, J. Stanger, M. Staiger, N.A. Hamid, P.L. Torres, The history of the science and technology of electrospinning from 1600 to 1995, Int. Symp. New Front. Fiber Mater. Sci. Conf. Proc. (2011).

[31] A. Haider, S. Haider, I.K. Kang, A comprehensive review summarizing the effect of electrospinning parameters and potential applications of nanofibers in biomedical and biotechnology, Arab. J. Chem. 11 (2018) 1165–1188. https://doi.org/10.1016/j.arabjc.2015.11.015.

[32] A. Formhals, Process and apparatus for preparing artificial threads, 1,975,504, 1934.

[33] N. Wang, Y. Si, J. Yu, H. Fong, B. Ding, Nano-fiber/net structured PVA membrane: Effects of formic acid as solvent and crosslinking agent on solution properties and membrane morphological structures, Mater. Des. 120 (2017) 135–

143. https://doi.org/10.1016/j.matdes.2017.02.007.

[34] D. Tian, C.-H. He, J.-H. He, Macromolecule Orientation in Nanofibers, Nanomaterials. 8 (2018) 918. https://doi.org/10.3390/nano8110918.

[35] T. Lin, X. Wang, Needleless Electrospinning of NanoFibers, Technology And Applications, CRC Press, 2013.

[36] N.M. Neves, Electrospinning for Advanced Biomedical Applications and Therapies, 2012. https://doi.org/10.1085/jgp.9.6.835.

[37] S.P. Miguel, D.R. Figueira, D. Simões, M.P. Ribeiro, P. Coutinho, P. Ferreira, I.J. Correia, Electrospun polymeric nanofibres as wound dressings: A review, Colloids Surfaces B Biointerfaces. 169 (2018) 60–71. https://doi.org/10.1016/j.colsurfb.2018.05.011.

[38] D.H. Reneker, A.L. Yarin, Electrospinning jets and polymer nanofibers, Polymer (Guildf). 49 (2008) 2387–2425. https://doi.org/10.1016/j.polymer.2008.02.002.

[39] Y. Xin, D.H. Reneker, Garland formation process in electrospinning, Polymer (Guildf). 53 (2012) 3629–3635. https://doi.org/10.1016/j.polymer.2012.05.060.

[40] W.E. Teo, R. Inai, S. Ramakrishna, Technological advances in electrospinning of nanofibers, Sci. Technol. Adv. Mater. 12 (2011). https://doi.org/10.1088/1468-6996/12/1/013002.

[41] S. Bagchi, R. Brar, B. Singh, C. Ghanshyam, Instability controlled synthesis of tin oxide nanofibers and their gas sensing properties, J. Electrostat. 78 (2015) 68–78. https://doi.org/10.1016/j.elstat.2015.11.001.

[42] N. Okutan, P. Terzi, F. Altay, Affecting parameters on electrospinning process and characterization of electrospun gelatin nanofibers, Food Hydrocoll. 39 (2014) 19–26. https://doi.org/10.1016/j.foodhyd.2013.12.022.

[43] A.L. Yarin, S. Koombhongse, D.H. Reneker, Taylor cone and jetting from liquid droplets in electrospinning of nanofibers, J. Appl. Phys. 90 (2001) 4836–4846. https://doi.org/10.1063/1.1408260.

[44] B.B. Wang, X.D. Wang, T.H. Wang, Microscopic mechanism for the effect of adding salt on electrospinning by molecular dynamics simulations, Appl. Phys. Lett. 105 (2014) 1–5. https://doi.org/10.1063/1.4896690.

[45] C. Zhang, S. Wu, J. Wu, D. Wu, X. Qin, Preparation and characterization of microporous sodium poly(aspartic acid) nanofibrous hydrogel, J. Porous Mater. 24

(2017) 75–84. https://doi.org/10.1007/s10934-016-0239-3.

[46] D. Barczikai, V. Kacsari, J. Domokos, D. Szabó, A. Jedlovszky-Hajdu, Interaction of silver nanoparticle and commonly used anti-inflammatory drug within a poly(amino acid) derivative fibrous mesh, J. Mol. Liq. 322 (2021). https://doi.org/10.1016/j.molliq.2020.114575.

[47] B. Song, W. Cui, J. Chang, Study on the effect of inorganic salts on the alignment of electrospun fiber, J. Appl. Polym. Sci. 122 (2011) 1047–1052. https://doi.org/10.1002/app.34197.

[48] Q. Zhang, M. Li, J. Liu, S. Long, J. Yang, X. Wang, Porous ultrafine fibers via a salt-induced electrospinning method, Colloid Polym. Sci. (2012). https://doi.org/10.1007/s00396-011-2563-0.

[49] M.A. Phadke, D.A. Musale, S.S. Kulkarni, S.K. Karode, Poly(acrylonitrile) ultrafiltration membranes. I. Polymer-salt-solvent interactions, J. Polym. Sci. Part B Polym. Phys. 43 (2005) 2061–2073. https://doi.org/10.1002/polb.20493.

[50] P. Su, C. Wang, X. Yang, X. Chen, C. Gao, X.X. Feng, J.Y. Chen, J. Ye, Z. Gou, Electrospinning of chitosan nanofibers: The favorable effect of metal ions, Carbohydr. Polym. 84 (2011) 239–246. https://doi.org/10.1016/j.carbpol.2010.11.031.

[51] D. Paneva, N. Manolova, I. Rashkov, H. Penchev, M. Mihai, E.S. Dragan, Self-organization of fibers into yarns during electrospinning of polycation/polyanion polyelectrolyte pairs, Dig. J. Nanomater. Biostructures. 5 (2010) 811–819.

[52] X.-H.H. Qin, E.-L.L. Yang, N. Li, S.-Y.Y. Wang, Effect of different salts on electrospinning of polyacrylonitrile (PAN) polymer solution, J. Appl. Polym. Sci. 103 (2007) 3865–3870. https://doi.org/10.1002/app.25498.

[53] A. Jedlovszky-Hajdu, K. Molnar, P.M. Nagy, K. Sinko, M. Zrinyi, Preparation and properties of a magnetic field responsive three-dimensional electrospun polymer scaffold, Colloids Surfaces A Physicochem. Eng. Asp. 503 (2016) 79–87. https://doi.org/10.1016/j.colsurfa.2016.05.036.

[54] X. Liu, T. Lin, J. Fang, G. Yao, H. Zhao, M. Dodson, X. Wang, In vivo wound healing and antibacterial performances of electrospun nanofibre membranes, J. Biomed. Mater. Res. - Part A. 94 (2010) 499–508. https://doi.org/10.1002/jbm.a.32718.

[55] C. Lu, P. Chen, J. Li, Y. Zhang, Computer simulation of electrospinning. Part I. Effect of solvent in electrospinning, Polymer (Guildf). 47 (2006) 915–921. https://doi.org/10.1016/j.polymer.2005.11.090.

[56] C. Voniatis, R. Gottscháll, D. Barczikai, G. Szabó, A. Jedlovszky-Hajdu, Enhancing critical features of poly(amino acid) based meshes, J. Appl. Polym. Sci. 139 (2022) 1–14. https://doi.org/10.1002/app.51933.

[57] X. Zong, K. Kim, D. Fang, S. Ran, B.S. Hsiao, B. Chu, Structure and process relationship of electrospun bioabsorbable nanofiber membranes, Polymer (Guildf). 43 (2002) 4403–4412. https://doi.org/10.1016/S0032-3861(02)00275-6.

[58] K.Y. Jeong, J.S. Lee, D.H. Paik, W.K. Jung, S.W. Choi, Fabrication of cell-penetrable microfibrous matrices with a highly porous structure using a simple fluidic device for tissue engineering, Mater. Lett. 168 (2016) 116–120. https://doi.org/10.1016/j.matlet.2016.01.045.

[59] A.M. Afifi, H. Nakajima, H. Yamane, Y. Kimura, S. Nakano, Fabrication of aligned poly(L-lactide) fibers by electrospinning and drawing, Macromol. Mater. Eng. 294 (2009) 658–665. https://doi.org/10.1002/mame.200900101.

[60] C.J. Luo, M. Nangrejo, M. Edirisinghe, A novel method of selecting solvents for polymer electrospinning, Polymer (Guildf). 51 (2010) 1654–1662. https://doi.org/10.1016/j.polymer.2010.01.031.

[61] A. Greiner, J.H. Wendorff, Electrospinning: A Fascinating Method for the Preparation of Ultrathin Fibers, Angew. Chemie Int. Ed. 46 (2007) 5670–5703. https://doi.org/10.1002/anie.200604646.

[62] A. Baji, Y.W. Mai, S.C. Wong, M. Abtahi, P. Chen, Electrospinning of polymer nanofibers: Effects on oriented morphology, structures and tensile properties, Compos. Sci. Technol. 70 (2010) 703–718. https://doi.org/10.1016/j.compscitech.2010.01.010.

[63] M.A. Alfaro De Prá, R.M. Ribeiro-do-Valle, M. Maraschin, B. Veleirinho, Effect of collector design on the morphological properties of polycaprolactone electrospun fibers, Mater. Lett. 193 (2017) 154–157. https://doi.org/10.1016/j.matlet.2017.01.102.

[64] S.M. Taghavi, R.G. Larson, Regularized thin-fiber model for nanofiber formation by centrifugal spinning, Phys. Rev. E - Stat. Nonlinear, Soft Matter Phys. 89 (2014)

1–9. https://doi.org/10.1103/PhysRevE.89.023011.

[65] H. Niu, T. Lin, Fiber generators in needleless electrospinning, J. Nanomater. 2012 (2012). https://doi.org/10.1155/2012/725950.

[66] R.R. Yang, J.H. He, J.Y. Yu, Effect of Solution Conductivity on the Morphology of Bubble-Electrospun Nanofibers, Adv. Mater. Res. 332–334 (2011) 1003–1006. https://doi.org/10.4028/www.scientific.net/amr.332-334.1003.

[67] J. Walser, S.J. Ferguson, Oriented nanofibrous membranes for tissue engineering applications: Electrospinning with secondary field control, J. Mech. Behav. Biomed. Mater. 58 (2016) 188–198. https://doi.org/10.1016/j.jmbbm.2015.06.027.

[68] M.M.L. Arras, C. Grasl, H. Bergmeister, H. Schima, Electrospinning of aligned fibers with adjustable orientation using auxiliary electrodes, Sci. Technol. Adv. Mater. 13 (2012). https://doi.org/10.1088/1468-6996/13/3/035008.

[69] K. Sarkar, C. Gomez, S. Zambrano, M. Ramirez, E. De Hoyos, H. Vasquez, K. Lozano, Electrospinning to Forcespinning™, Mater. Today. 13 (2010) 12–14. https://doi.org/10.1016/S1369-7021(10)70199-1.

[70] Y. Kara, H. He, K. Molnár, Shear-aided high-throughput electrospinning: A needleless method with enhanced jet formation, J. Appl. Polym. Sci. 137 (2020) 1–13. https://doi.org/10.1002/app.49104.

[71] Q.C. Zhang, L.H. Wang, Z.M. Wei, X.J. Wang, S.R. Long, J. Yang, Large-scale aligned fiber mats prepared by salt-induced pulse electrospinning, J. Polym. Sci. Part B-Polymer Phys. 50 (2012) 1004–1012. https://doi.org/Doi 10.1002/Polb.23096.

[72] J. Yao, C. Bastiaansen, T. Peijs, High Strength and High Modulus Electrospun Nanofibers, Fibers. 2 (2014) 158–186. https://doi.org/10.3390/fib2020158.

[73] Z. Ouyang, J. Li, J. Wang, Q. Li, T. Ni, X. Zhang, H. Wang, Q. Li, Z. Su, G. Wei, Fabrication, characterization and sensor application of electrospun polyurethane nanofibers filled with carbon nanotubes and silver nanoparticles, J. Mater. Chem. B. 1 (2013) 2415–2424. https://doi.org/10.1039/c3tb20316f.

[74] Y.H. Lee, J.H. Lee, I.G. An, C. Kim, D.S. Lee, Y.K. Lee, J. Do Nam, Electrospun dual-porosity structure and biodegradation morphology of Montmorillonite reinforced PLLA nanocomposite scaffolds, Biomaterials. 26 (2005) 3165–3172. https://doi.org/10.1016/j.biomaterials.2004.08.018.

[75] M. Vong, E. Speirs, C. Klomkliang, I. Akinwumi, W. Nuansing, N. Radacsi, Controlled three-dimensional polystyrene micro- and nano-structures fabricated by three-dimensional electrospinning, RSC Adv. 8 (2018) 15501–15512. https://doi.org/10.1039/c7ra13278f.

[76] S. Lee, M.K. Joshi, A.P. Tiwari, B. Maharjan, K.S. Kim, Y.H. Yun, C.H. Park, C.S. Kim, Lactic acid assisted fabrication of bioactive three-dimensional PLLA/B-TCP fibrous scaffold for biomedical application, Chem. Eng. J. 347 (2018) 771–781. https://doi.org/10.1016/j.cej.2018.04.158.

[77] Y. Liu, R. Liu, X. Wang, J. Jiang, W. Li, J. Liu, S. Guo, G. Zheng, Electrospun Three-Dimensional Nanofibrous Structure via Probe Arrays Inducing, Micromachines. 9 (2018) 427. https://doi.org/10.3390/mi9090427.

[78] C. Froese Fischer, General Hartree-Fock program, Comput. Phys. Commun. 43 (1987) 355–365. https://doi.org/10.1016/0010-4655(87)90053-1.

[79] R.J. Bartlett, J.F. Stanton, Applications of Post-Hartree-Fock Methods: A Tutorial, Rev. Comput. Chem. 5 (2007) 65–169. https://doi.org/10.1002/9780470125823.ch2.

[80] M. Chen, H.Y. Ko, R.C. Remsing, M.F. Calegari Andrade, B. Santra, Z. Sun, A. Selloni, R. Car, M.L. Klein, J.P. Perdew, X. Wu, Ab initio theory and modeling of water, Proc. Natl. Acad. Sci. U. S. A. 114 (2017) 10846–10851. https://doi.org/10.1073/pnas.1712499114.

[81] J.A. Pople, P. V. Schleyer, W.J. Hehre, L. Radom, AB INITIO molecular orbital theory, AB INITIO Mol. Orbital Theory. 9 (1986). https://doi.org/10.1016/s0022-328x(00)99651-7.

[82] I.A. Boyarskaya, S.K. Akopyan, Quantum-chemical calculation of spectral characteristics and structure of complexes [Mg(DMF) i (CH3CN)6-i]2+ and IR spectra of the tricomponent solutions Mg(ClO4) 2-DMF-CH3CN, Russ. J. Gen. Chem. 78 (2008) 2317–2329. https://doi.org/10.1134/S1070363208120050.

[83] K. Fujii, H. Wakamatsu, Y. Todorov, N. Yoshimoto, M. Morita, Structural and Electrochemical Properties of Li Ion Solvation Complexes in the Salt-Concentrated Electrolytes Using an Aprotic Donor Solvent, N,N-Dimethylformamide, J. Phys. Chem. C. 120 (2016) 17196–17204. https://doi.org/10.1021/acs.jpcc.6b04542.

[84] M.B. Shundalau, P.S. Chybirai, A.I. Komyak, A.P. Zazhogin, M.A. Ksenofontov, D.S. Umreiko, Modeling of structures and calculation of IR vibrational spectra of N,N-dimethylformamide dimers by density functional theory, J. Appl. Spectrosc. 78 (2011) 326–336. https://doi.org/10.1007/s10812-011-9466-1.

[85] K. Burke, L.O. Wagner, DFT in a nutshell, Int. J. Quantum Chem. 113 (2013) 96–101. https://doi.org/10.1002/qua.24259.

[86] O.Y. Kweon, S.J. Lee, J.H. Oh, Wearable high-performance pressure sensors based on three-dimensional electrospun conductive nanofibers, NPG Asia Mater. 10 (2018) 540–551. https://doi.org/10.1038/s41427-018-0041-6.

[87] A. Shastri, A.K. Das, S. Krishnakumar, P.J. Singh, B.N. Raja Sekhar, Spectroscopy of N, N -dimethylformamide in the VUV and IR regions: Experimental and computational studies, J. Chem. Phys. 147 (2017). https://doi.org/10.1063/1.5006126.

[88] Y. Zhao, D.G. Truhlar, The M06 suite of density functionals for main group thermochemistry , thermochemical kinetics , noncovalent interactions , excited states , and transition elements : two new functionals and systematic testing of four M06-class functionals and 12 other fun, (2008) 215–241. https://doi.org/10.1007/s00214-007-0310-x.

[89] et al. G.E.S.M.J. Frisch, G.W. Trucks, H.B. Schlegel, Gaussian 16, Revision A.03, (2016).

[90] J.G. Kirkwood, E.M. Boggs, The radial distribution function in liquids, J. Chem. Phys. 10 (1942) 394–402. https://doi.org/10.1063/1.1723737.

[91] W. Brostow, Radial distribution function peaks and coordination numbers in liquids and in amorphous solids, Chem. Phys. Lett. 49 (1977) 285–288. https://doi.org/10.1016/0009-2614(77)80588-5.

[92] J.M. Kincaid, J.J. Weis, Radial distribution function of a hard-sphere solid, Mol. Phys. 34 (1977) 931–938. https://doi.org/10.1080/00268977700102241.

[93] V. Koverga, Á. Juhász, D. Dudariev, M. Lebedev, A. Idrissi, P. Jedlovszky, Local Structure of DMF-Water Mixtures, as Seen from Computer Simulations and Voronoi Analysis, J. Phys. Chem. B. 126 (2022) 6964–6978. https://doi.org/10.1021/acs.jpcb.2c02235.

[94] A. Idrissi, P. Damay, M. Kiselev, Nearest neighbor assessments of spatial

distribution in CO2: A molecular dynamics analysis, Chem. Phys. 332 (2007) 139–143. https://doi.org/10.1016/j.chemphys.2006.11.037.

[95] M.D. Elola, B.M. Ladanyi, Computational study of structural and dynamical properties of formamide-water mixtures, J. Chem. Phys. 125 (2006). https://doi.org/10.1063/1.2364896.

[96] A. Idrissi, B. Marekha, M. Kiselev, P. Jedlovszky, The local environment of the molecules in water-DMSO mixtures, as seen from computer simulations and Voronoi polyhedra analysis, Phys. Chem. Chem. Phys. 17 (2015) 3470–3481. https://doi.org/10.1039/c4cp04839c.

[97] P. Jedlovszky, Voronoi polyhedra analysis of the local structure of water from ambient to supercritical conditions, J. Chem. Phys. 111 (1999) 5975–5985. https://doi.org/10.1063/1.479893.

[98] W. Brostow, M. Chybicki, R. Laskowski, J. Rybicki, Voronoi polyhedra and Delaunay simplexes in the structural analysis of molecular-dynamics-simulated materials, Phys. Rev. B - Condens. Matter Mater. Phys. 57 (1998) 13448–13458. https://doi.org/10.1103/PhysRevB.57.13448.

[99] F. Menges, Spectragryph - optical spectroscopy software, (n.d.).

[100] P. Jedlovszky, L. Turi, Role of the C-H···O hydrogen bonds in liquids: A Monte Carlo simulation study of liquid formic acid using a newly developed pair-potential, J. Phys. Chem. B. 101 (1997) 5429–5436. https://doi.org/10.1021/jp963906t.

[101] B. Scrosati, C. Vincent, Alkali Metal, Alkaline Earth Metal and Ammonium Halides, Amide Solvents, Iupac Sds. 11 (1980). https://doi.org/10.1016/0021-9614(80)90193-7.

[102] Y. Lei, H. Li, H. Pan, S. Han, Structures and Hydrogen Bonding Analysis of N , N -Dimethylformamide and, J. Phys. Chem. A. (2003) 1574–1583.

[103] A. Idrissi, K. Polok, W. Gadomski, I. Vyalov, A. Agapov, M. Kiselev, M. Barj, P. Jedlovszky, Detailed insight into the hydrogen bonding interactions in acetone-methanol mixtures. A molecular dynamics simulation and Voronoi polyhedra analysis study, Phys. Chem. Chem. Phys. 14 (2012) 5979–5987. https://doi.org/10.1039/c2cp24101c.

[104] C.J. Angammana, Thesis: A Study of the Effects of Solution and Process

Parameters on the Electrospinning Process and Nanofibre Morphology, 47 (2011) 1109–1117.

[105] G. Kabisch, E. Kálmán, G. Pálinkás, T. Radnai, F. Gaizer, Complex formation and solvation of zinc bromide in N,N-dimethylformamide solution: An electron diffraction and Raman study, Chem. Phys. Lett. 107 (1984) 463–468. https://doi.org/10.1016/S0009-2614(84)80256-0.

[106] D.W. James, R.E. Mayes, Ion-ion-solvent interactions in solution. 8. Spectroscopic studies of the lithium perchlorate/N,N-dimethylformamide system, J. Phys. Chem. 88 (1984) 637–642. https://doi.org/10.1021/j150647a058.

[107] M. Bradley, Curve Fitting in Raman and IR Spectroscopy: Basic Theory of Line Shapes and Applications, Appl. Note 50733. (2007) 0–3. https://doi.org/10.1002/2015JG003204.Received.

[108] Y. Umebayashi, K. Matsumoto, M. Watanabe, K. Katoh, S.I. Ishiguro, Individual solvation numbers around the nickel(II) ion in an N,N-dimethylformamide and N,N-dimethylacetamide mixture determined by Raman spectrophotometry, Anal. Sci. 17 (2001) 323–326. https://doi.org/10.2116/analsci.17.323.

[109] J.D. Forero-Saboya, E. Marchante, R.B. Araujo, D. Monti, P. Johansson, A. Ponrouch, Cation Solvation and Physicochemical Properties of Ca Battery Electrolytes, J. Phys. Chem. C. 123 (2019) 29524–29532. https://doi.org/10.1021/acs.jpcc.9b07308.

[110] W.E. Waghorne, H. Rubalcava, Infrared spectroscopic study of the effects of different cations on NN-dimethylacetamide and fully deuterated NN-dimethylformamide, J. Chem. Soc. Faraday Trans. 1 Phys. Chem. Condens. Phases. 78 (1982) 1199–1207. https://doi.org/10.1039/F19827801199.

[111] Y. Umebayashi, B. Mroz, M. Asada, K. Fujii, K. Matsumoto, Y. Mune, M. Probst, S.I. Ishiguro, Conformation of solvent N,N-dimethylpropionamide in the coordination sphere of the Zinc(II) ion studied by Raman spectroscopy and DFT calculations, J. Phys. Chem. A. 109 (2005) 4862–4868. https://doi.org/10.1021/jp044763a.

[112] K. Fujii, M. Sogawa, N. Yoshimoto, M. Morita, Structural Study on Magnesium Ion Solvation in Diglyme-Based Electrolytes: IR Spectroscopy and DFT Calculations, J. Phys. Chem. B. 122 (2018) 8712–8717.

https://doi.org/10.1021/acs.jpcb.8b05586.

[113] B. Zhang, Y. Zhou, X. Li, J. Wang, G. Li, Q. Yun, X. Wang, Li+-molecule interactions of lithium tetrafluoroborate in propylene carbonate + N,N-dimethylformamide mixtures: An FTIR spectroscopic study, Spectrochim. Acta - Part A Mol. Biomol. Spectrosc. 124 (2014) 40–45. https://doi.org/10.1016/j.saa.2014.01.001.

[114] C.P. Rao, A.M. Rao, C.N.R. Rao, Crystal and Molecular Structures of Alkali-and Alkaline-Earth-Metal Complexes of N,N-Dimethylformamide, Inorg. Chem. 23 (1984) 2080–2085.

[115] W. Hu, Z. Wang, Y. Xiao, S. Zhang, J. Wang, Advances in crosslinking strategies of biomedical hydrogels, Biomater. Sci. 7 (2019) 843–855. https://doi.org/10.1039/c8bm01246f.

[116] K.D. Collins, Ion hydration: Implications for cellular function, polyelectrolytes, and protein crystallization, Biophys. Chem. 119 (2006) 271–281. https://doi.org/10.1016/j.bpc.2005.08.010.

[117] L. Guo, W. Gu, C. Peng, W. Wang, Y. Jie Li, T. Zong, Y. Tang, Z. Wu, Q. Lin, M. Ge, G. Zhang, M. Hu, X. Bi, X. Wang, M. Tang, A comprehensive study of hygroscopic properties of calcium-and magnesium-containing salts: Implication for hygroscopicity of mineral dust and sea salt aerosols, Atmos. Chem. Phys. 19 (2019) 2115–2133. https://doi.org/10.5194/acp-19-2115-2019.

[118] S. Bouzenada, A.N. Kaabi, L. Frainkin, T. Salmon, A. Léonard, Experimental Comparative Study on Lithium Chloride and Calcium Chloride Desiccants, Procedia Comput. Sci. 83 (2016) 718–725. https://doi.org/10.1016/j.procs.2016.04.159.

[119] K. Arayanarakul, N. Choktaweesap, D. Aht-ong, C. Meechaisue, P. Supaphol, Effects of poly(ethylene glycol), inorganic salt, sodium dodecyl sulfate, and solvent system on electrospinning of poly(ethylene oxide), Macromol. Mater. Eng. 291 (2006) 581–591. https://doi.org/10.1002/mame.200500419.

[120] C. Mit-Uppatham, M. Nithitanakul, P. Supaphol, Ultrafine electrospun polyamide-6 fibers: Effect of solution conditions on morphology and average fiber diameter, Macromol. Chem. Phys. 205 (2004) 2327–2338. https://doi.org/10.1002/macp.200400225.

10 Bibliography of the candidate's publications – related to the thesis

[JAGy1] Koverga, Volodymyr ; Juhász, Ákos ; Dudariev, Dmytro ; Lebedev, Maxim ; Idrissi, Abdenacer ; Jedlovszky, Pál: Local Structure of DMF–Water Mixtures, as Seen from Computer Simulations and Voronoi Analysis, JOURNAL OF PHYSICAL CHEMISTRY B 126 : 36 pp. 6964-6978. , 15 p. (2022) [93]

[JAGy2] Juhász, Ákos György; Molnar, Kristof ; Idrissi, Abdenacer ; Jedlovszky-Hajdu, Angela: Salt induced fluffy structured electrospun fibrous matrix, JOURNAL OF MOLECULAR LIQUIDS 312 Paper: 113478 , 10 p. (2020) [24]

11 Bibliography of the candidate's publications – not related to the thesis

1. Tóth, Krisztina ; S Nagy, Krisztina ; Güler, Zeliha ; Juhász, Ákos György ; Pállinger, Éva ; Varga, Gábor ; Sarac, A Sezai ; Zrínyi, Miklós ; Jedlovszky-Hajdú, Angéla ; Juriga, Dávid: Characterization of Electrospun Polysuccinimide-dopamine Conjugates and Effect on Cell Viability and Uptake, MACROMOLECULAR BIOSCIENCE in press Paper: e2200397 , 16 p. (2023)
2. Juhász, Ákos György: Az elektromos szálhúzás technikájának bemutatása, KALEIDOSCOPE: MŰVELŐDÉS- TUDOMÁNY- ÉS ORVOSTÖRTÉNETI FOLYÓIRAT 11 : 23 pp. 236-247. , 12 p. (2021)
3. Marekha, Bogdan A. ; Koverga, Volodymyr ; Maity, Nishith ; Juhasz, Akos ; Miannay, François A. ; Inkol, Anton ; Takamuku, Toshiyuki ; Jedlovszky, Pal ; Kalugin, Oleg N. ; Idrissi, Abdenacer: Local Structure in Mixtures of Ionic Liquid with Molecular Solvent: Vibration Spectroscopy, NMR and Molecular Dynamics Simulation, In: Yoshida, Norio; Takamuku, Toshiyuki; Yamaguchi, Tsuyoshi; Nishiyama, Katsura (szerk.) Molecular Basics of Liquids and Liquid-Based Materials, Springer Singapore (2021) pp. 289-334. , 46 p.
4. Sipos, Evelin ; Juhasz, Akos ; Zrinyi, Miklos: Characteristic load-elongation behavior of weak electrospun fiber texture, JOURNAL OF MOLECULAR LIQUIDS 329 Paper: 115459 , 11 p. (2021)
5. Koverga, Volodymyr ; Maity, Nishith ; Miannay, Francois Alexandre ; Kalugin, Oleg N. ; Juhasz, Akos ; Swiatek, Adam ; Polok, Kamil ; Takamuku, Toshiyuki ; Jedlovszky, Pal ; Idrissi, Abdenacer: Voronoi Polyhedra as a Tool for the Characterization of Inhomogeneous Distribution in 1-Butyl-3-methylimidazolium Cation-Based Ionic Liquids, JOURNAL OF PHYSICAL CHEMISTRY B 124 : 46 pp. 10419-10434. , 16 p. (2020)
6. Hegedűs, Orsolya ; Juriga, Dávid ; Sipos, Evelin ; Voniatis, Constantinos ; Juhász, Ákos ; Idrissi, Abdenaccer ; Zrínyi, Miklós ; Varga, Gábor ; Jedlovszky-Hajdú, Angéla ; S. Nagy, Krisztina: Free thiol groups on poly(aspartamide) based hydrogels facilitate tooth-derived progenitor cell proliferation and differentiation, PLOS ONE 14 : 12 Paper: e0226363 , 20 p. (2019)
7. Jedlovszky-Hajdú, Angéla ; Juhász, Ákos György ; Szakál, Tímea ; Molnár, Kristóf: Ezüst tartalmú nanoszálak előállítása potenciális sebfedőként, In: Nagy, Noémi; Tóbi, István (szerk.) (2017) 296 p. pp. 104-110. , 7 p.

12 Acknowledgment

I will be forever grateful to Angéla Jedlovszky-Hajdú and Nacer Idrissi for your trust and support during these years. While it was not an easy ride, you always put me on the right track. You have taught me a lot about science and life. I'm very fortunate that I met you and I could have worked with you. Thank you!!!

I would also like to thank Prof. Miklós Kellermayer and Prof. Miklós Zrínyi for giving me a place on the research team over the years. Special thanks to Kristóf Molnár who shared with me his knowledge, introduced me to laboratory research, and to this date still eagerly awaiting my questions. I would like to thank also Prof. László Smeller for giving me careful and insightful advices.

I would like to thank the kindness to all the members of the Nanochemistry Group especially Dávid Juriga, Krisztina Tóth, Constantinos Voniatis, Rita Pázmány and Forró Evelin who have always been available for working on something or just to have discussion over a coffee.

I would like to thank also the LASIRe lab of University of Lille and Hervé Vezin for providing me a place for my PhD and to the help for the countless measurements I did there. I'm grateful for the help with the spectroscopy measurement to Isabelle De Waele and Myriam Moreau, and also for the help with the SEM to Alexandre Fadel. I would like to thank to all the members of the lab for their kindness, especially to Alessandro Nardecchia, Bálint Kiss and Yevhenii Vaksler who were always eager for a discussion with a coffee break or a night's out.

I would like to specially thank for Campus France for providing me financial support for the cotutelle programme. I feel extremely fortunate to have participated in this programme. I would like to thank my friends especially Péter Csuhaj, Ráhel Horváth and Zsolt Laczkó who have never doubted me that I have to step on this path, and always showing me the true face of life even when it's hard to accept. Special thanks to Claudia and Pál, who also were very kind to me all these years and helped me with all kinds of things when I needed. I'm very fortunate to met you as well.

Lastly, I will be forever grateful for the constant support from my family, especially my parents. They also never had doubts in me. At least, I hope. They tried to shape me, showing me to always be better and never give up. I know I wasn't easy to handle, but I'll never forget the love and support throughout all these years.